



A Cohesive Element-Based Numerical Manifold Method for Hydraulic Fracturing Modelling with Voronoi Grains

Zhijun Wu¹ · Hao Sun¹ · Louis Ngai Yuen Wong²

Received: 17 August 2018 / Accepted: 19 December 2018 / Published online: 2 January 2019
© Springer-Verlag GmbH Austria, part of Springer Nature 2019

Abstract

In this study, the cohesive element-based numerical manifold method with Voronoi grains is extended by incorporating a coupled hydro-mechanical (HM) model to investigate hydraulic fracturing of rock at micro-scale. The proposed hydraulic solving framework, which explicitly calculates the flow rate and fluid pressure of a compressible viscous fluid based on the cubic law and a linear fluid compressibility model, is first validated against analytical solutions for uncoupled transient and steady flow examples. Then the coupled HM procedure is further verified by two coupled examples, which respectively considers the elastic response of a pressurized fracture and hydraulic fracture (HF) propagation under different perforation inclinations and in situ stresses. Finally, the developed method is adopted to investigate the hydraulic fracture propagation in Augig granite possessing multi-fractures at micro-scale, based on which the effect of friction coefficient of natural fractures (NFs) on hydraulic fracture propagation is examined. The results show that the friction coefficient of the NFs has significant effects on the induced hydraulic fracture pattern. With increasing friction coefficient of the NFs, it becomes more difficult for the NFs to fail, which results in simpler HF patterns. This phenomenon is associated with the change in the type of interaction between HFs and NFs, i.e., from HFs being arrested by NFs to HFs crossing the NFs with offsets and then to HFs directly crossing NFs.

Keywords Numerical manifold method · Coupled hydro-mechanical model · Micro-structure · Hydraulic fracturing · Cohesive element

List of Symbols

E Young's modulus of the granite sample
 ν Poisson's ratio
 ρ Bulk density of the rock material
 M_i Mathematical patch numbered i
 P_i Physical patch numbered i
 E_i Manifold element numbered i
 G_I Mode-I fracture energy
 G_{II} Mode-II fracture energy
 σ_t Tensile stress of cohesive element
 τ Shear stress of cohesive element
 c Shear cohesion of cohesive element
 σ_n Compressive stress of cohesive element
 D_o Mode-I damage factor

D_s Mode-II damage factor
 f_s Shear strength of the rock material
 f_t Tensile strength of the rock material
 O_p Critical opening displacement
 O_r Residual opening displacement
 S_p Critical sliding displacement
 S_r Residual sliding displacement
 w Relative normal displacement of the contact pair
 s Relative tangential displacement of the contact pair
 φ Friction angle of the contact interface
 V Volume of node
 a Equivalent hydraulic aperture
 q_{ij} Flow rate from node i to j
 μ Dynamic viscosity of the fluid
 ρ_f Fluid density
 g Acceleration of gravity
 S_i Saturation of the node i
 V_f Volume of fluid inside the node i
 K_f Bulk modulus of fluid
 k Intrinsic hydraulic conductivity
 N_i Natural fracture numbered i

✉ Louis Ngai Yuen Wong
Inyung@hku.hk

¹ School of Civil Engineering, Wuhan University,
Wuhan 430072, China

² Department of Earth Sciences, The University of Hong
Kong, Pokfulam, Hong Kong

p_{fn}	Normal penalty parameters
p_{ft}	Tangential penalty parameters
p_n	Normal contact penalty
p_t	Tangential contact penalty
φ_f	Friction angle of fracture

1 Introduction

Hydraulic fracturing is a typical coupled hydro-mechanical (HM) process, which has been widely used in many industries, especially unconventional oil and gas exploitation. To enhance the permeability of the rock masses during unconventional oil/gas exploitation, hydraulic fracturing is usually applied to generate new fractures to form a complex fracture network as a result of the activation of pre-existing natural fractures (NFs). This coupled HM problem involves the deformation of rocks and fractures, fluid flow in fractures, fracture propagation, and the interaction between hydraulically induced and natural fractures. At the microscopic scale, rock is made up of mineral grains and is characterized by different micro-structures and grain–grain interfaces. Therefore, to better understand the coupled mechanism of hydraulic fracturing, it is necessary to take the rock micro-structures, as well as their interactions with the fracturing fluid into consideration. However, due to the complex nature of rock micro-structures and the hydraulic fracturing process, realistically reflecting the micro-mechanism behind the coupled process of hydraulic fracturing is still challenging.

Terzaghi (1951) proposed the effective stress principle and the one-dimensional theory of consolidation to describe the coupled HM behavior of a porous medium (mainly soil) at early times. Based on Terzaghi's study, Biot and Willis (1957) introduced a theory of poroelasticity that used the theory of elasticity and Darcy's law for the description of solid behavior and interstitial fluid flow, respectively. Later, to account for more complicated conditions, such as pre-existing discontinuities and fracturing, Biot's theory was extended, and several improved analytical coupled HM methods were proposed (Bai et al. 1995; Detournay and Cheng 1988; Rudnicki 1985). With the extensive application of hydraulic fracturing in the petroleum industry, several analytical models of hydraulic fracturing, such as PKN (Nordgren 1972; Perkins and Kern 1961) and KGD (Geertsma and de Klerck 1969; Khristianovic and Zheltov 1955), have also been proposed based on different assumptions regarding the fracture geometry and the fluid pressure distribution inside the fractures. However, to realistically account for the complex model geometry and boundary conditions in hydraulic fracturing, the capabilities of existing analytical methods are not adequate.

Numerical methods, which conveniently deal with hydro-mechanical coupling under complex conditions, can

be classified as (1) continuum-based methods, (2) discontinuum-based methods and (3) hybrid methods. The finite element method (FEM) (Goodman 1976; Hu et al. 2014; Li et al. 2017; Weng et al. 2017) is a representative continuum-based methods that usually models coupled HM problems by treating a discontinuous rock mass as an equivalent-continuum medium. However, during the fracture propagation process, remeshing is required to make the fracture coincide with the finite element mesh, which demands an excessively high computational overhead. To overcome this deficiency of the FEM, the extended finite element method (XFEM) (Belytschko and Black 1999; Zhou and Cheng 2017) simulates fracture propagation by introducing an appropriate enrichment function. However, it is very difficult to define this function, in particular, for the branch-fracturing or multi-fracture problems. In addition to FEM-based methods, the displacement discontinuity method (DDM) (Cheng et al. 2017; Xie et al. 2016) is also widely used in hydraulic fracturing simulation but deficient in dealing with contact problems of closed fractures. Besides the conventional continuum methods described above, phase-field (Xia et al. 2017), peridynamics (Ren et al. 2016; Wang et al. 2018; Zhou et al. 2018) and meshfree method (Rabczuk and Belytschko 2004; Zhuang et al. 2012) were also recently introduced to tackle with the hydraulic fracturing problems. However, for continuum-based methods, considering the rock micro-structure, as well as its interaction during hydraulic fracturing modeling is still difficult.

Discontinuum-based methods such as discrete element methods (DEMs), which treat the rock mass as an assembly of separate blocks or particles, can easily deal with hydraulic fracturing in discontinuous rock masses at micro-scale by introducing a contact model between blocks or particles, as well as a coupled HM model. Among DEMs, the particle flow code (PFC) (Zhou et al. 2016, 2017), which represents a rock mass by bonded circular (2D) or spherical (3D) particles, is one of the most widely used methods for simulating hydraulic fracturing. However, circular or spherical particles cannot represent realistic rock micro-structures and will significantly reduce the interlocking effect of real rock grains. In addition, calibrating the micro-parameters required by PFC is challenging (Zhang and Wong 2018). Another circular particle-based flow-coupled DEM code was developed by Shimizu et al. (2011) to study the influence of the fluid viscosity and the particle size distribution on hydraulic fracturing in hard rock, and it was later used to investigate the effect of brittleness on the complexity of hydraulic fracture (Shimizu et al. 2018). Developed from PFC, the lattice model, which uses a lattice representation of the rock matrix with quasi-randomly distributed nodes connected by springs, is coupled with fluid flow to model hydraulic fracture containment in layered reservoirs (Damjanac and Cundall 2016; Xing et al. 2018). Different from

PFC, the distinct element code (UDEC/3DEC) (Chen et al. 2018; Damjanac and Cundall 2016; Zhao et al. 2015) adopts polygonal or polyhedral blocks bonded by virtual joints to simulate hydraulic fracturing. In addition to explicit DEMs summarized above, several coupled HM models were also proposed based on the implicit DEM discontinuous deformation analysis (DDA) (Jiao et al. 2015b; Ning and Zhao 2013; Shi and Goodman 1985) to represent the hydraulic fracturing process (Choo et al. 2016; Jiao et al. 2015a; Jing et al. 2001; Morgan and Aral 2015).

Due to the complex continuum–discontinuum characteristics of rock, several hybrid methods such as the finite–discrete element method (FDEM) (Lisjak et al. 2013; Mahabadi et al. 2012; Yan and Jiao 2018) and the numerical manifold method (NMM) (Li et al. 2018; Ma et al. 2009; Ning et al. 2017; Wu et al. 2017; Zhang et al. 2010; Zhao et al. 2014; Zheng and Xu 2014) were proposed to study the mechanical behavior and fracture propagation in rock. By incorporating coupled HM model into the FDEM, two fully coupled implementations respectively named Y-flow (Yan et al. 2015) and Irazu (Lisjak et al. 2017) were developed to investigate hydraulic fracturing in porous rock masses. However, the solid elements of the two implementations were both limited to triangular finite elements, which are incapable of realistically modelling the rock micro-structure. The NMM (Ma et al. 2010), which combines the continuum-based method FEM and discontinuum-based method DDA in a uniform framework, has been successfully applied to solve rock fracture related problems. By coupling the linear elastic fracture mechanics with a fluid flow model, the NMM has been successfully extended for modelling hydraulic fracture related problems at macro-scale (Hu et al. 2017a, b; Wu and Wong 2014; Yang et al. 2018).

As a composite material composed of grains, the mechanical and failure behavior and hydraulic fracturing behavior of rock are profoundly affected by its micro-structure. To more realistically and efficiently model the rock mechanical behavior at micro-scale, the Voronoi tessellation technique and zero thickness cohesive elements were incorporated into NMM (Co-NMM) by Wu et al. (2017) to construct random polygonal rock micro-grains and capture the interactions between the grains, respectively. Although Co-NMM can represent the rock micro-structure well and be used to investigate the micro-mechanisms underlying the macroscopic response and fracture processes in rock, without coupling the fluid flow model, it is incapable of solving coupled HM problems.

In view of the issues presented above, this study proposes a fully coupled HM formulation based on Co-NMM to model hydraulic fracturing under the influence of the rock micro-structure. A comprehensive validation of the coupled HM procedure against analytical solutions as well as experimental results is presented, including coupled and uncoupled

examples. The proposed hydraulic solving framework is first verified using uncoupled examples, which analyse transient and steady flows through fractures with constant and uniform apertures. In addition, two coupled examples, which respectively consider the elastic responses of a pressurized fracture and hydraulic fracture propagation under different perforation inclinations and in situ stresses, are then adopted to validate the coupled HM approach. Finally, the coupled HM procedure is further applied to model hydraulic fracturing in Augig granite (AG) possessing multi-fractures, based on which the effect of the friction coefficient of natural fractures (NFs) on hydraulic fracture propagation is examined and discussed. The results illustrate that the developed method can well model the hydraulic fracture propagation processes at micro-scale, which involves correctly modelling the fluid flow in fractures, fracture propagation, and interactions among the rock micro-structure, fracturing fluid as well as hydraulic induced and natural fractures.

2 Fundamental Principles of Co-NMM

This section presents the procedures used by Co-NMM to realistically model rock mechanical behavior at micro-scale. In Co-NMM, using the Voronoi tessellation technique, the rock specimen is first discretized into several independent loops (grains), which define the shapes and boundaries of the rock grains as well as the contacts between them. Each grain consists of several manifold elements, which control the mechanical behavior of the rock grain itself. Then, based on the formed Voronoi grains, zero thickness cohesive elements with a stress–displacement constitutive model are embedded between adjacent grains to capture the interaction between the grains before failure. To more efficiently capture the contact behavior between the rock grains after failure, a grain based contact algorithm is adopted, which allows a smooth transition from the cohesive element to the contact model during fracturing process. In the following sections, the basic background of Co-NMM is presented, and the generation of the rock micro-structure is then introduced along with the contact mechanics.

2.1 Finite Cover System

The core and most innovative characteristic of Co-NMM inherited from the original NMM is the two cover (mesh) system, which includes the mathematical cover (MC) and physical cover (PC). The mathematical cover, which is a set of user-defined overlapping unions of arbitrarily shaped mathematical patches, must be large enough to cover the entire physical domain. The physical cover consists of all of the physical patches that are obtained by intersecting the mathematical patches with the physical components of the

problem domain. Here, the physical components of the problem domain include the problem domain boundaries, block boundaries, material interfaces, holes and discontinuities. Each mathematical patch is divided into at least one physical patch, the common regions of which form the manifold elements (MEs) in Co-NMM.

The basic construction procedures of the finite covering system described above are illustrated in Fig. 1. The problem domain is completely covered by the mathematical cover, which consists of two mathematical patches (the circular patch M_1 and the rectangular patch M_2), and the physical components of the problem domain contain a physical

boundary Γ_u and a discontinuity Γ_D . Then, by intersecting the mathematical patches with the physical components for example, intersecting the mathematical patch M_1 with the physical boundary Γ_u and the discontinuity Γ_D forms the physical patches P_{1-1} and P_{1-2} , while intersecting the mathematical patch M_2 with the physical boundary Γ_u forms physical patch P_{2-1} . Finally, by overlapping these formed physical patches, the MEs are generated; for example, elements E_3 and E_4 are formed from the common area of P_{1-1} and P_{2-1} and that of P_{1-2} and P_{2-1} , respectively, and elements E_1, E_2 and E_5 are respectively formed from the remaining independent areas of the physical patches as shown in Fig. 1.

Based on the independent definition of the local approximation functions $u_i^h(r)$ on each physical patch P_i , the global displacement function for each ME can be obtained by connecting the local approximation functions together as:

$$u^h(r) = \sum_{i=1}^n w_i(r)u_i^h(r), \tag{1}$$

where r denotes the position vector, n is the number of physical patches, and $w_i(r)$ is the weight function of P_i , which should satisfy:

$$\left. \begin{aligned} w_i(r) &\geq 0 \quad \forall r \in P_i \\ w_i(r) &= 0 \quad \forall r \notin P_i \\ \sum_{r \in P_i} w_i(r) &= 1 \end{aligned} \right\} \tag{2}$$

Due to the adoption of a regular triangular mesh and a linear displacement approximation, which respectively form the mathematical cover and displacement functions of the manifold elements in this study, the weighting functions are equal to the shape functions of the three-node triangular finite element.

By taking the two cover system, the displacement jump across the discontinuity can be simply captured without further enrichments; for example, the jump across interface Γ_D between elements E_3 and E_4 in Fig. 1 can be calculated as follows.

First, the displacements of E_3 and E_4 can be expressed respectively as:

$$\begin{cases} u_{E_3}^h(r) = w_{P_{1-1}}(r)u_{P_{1-1}}^h(r) + w_{P_{2-1}}(r)u_{P_{2-1}}^h(r) \\ u_{E_4}^h(r) = w_{P_{1-2}}(r)u_{P_{1-2}}^h(r) + w_{P_{2-1}}(r)u_{P_{2-1}}^h(r) \end{cases} \tag{3}$$

Then, the displacement jump across interface Γ_D between elements E_3 and E_4 can be obtained as:

$$u_{\Gamma_D}(r) = u_{E_3}^h(r) - u_{E_4}^h(r) = w_{P_{1-1}}(r)u_{P_{1-1}}^h(r) - w_{P_{1-2}}(r)u_{P_{1-2}}^h(r). \tag{4}$$

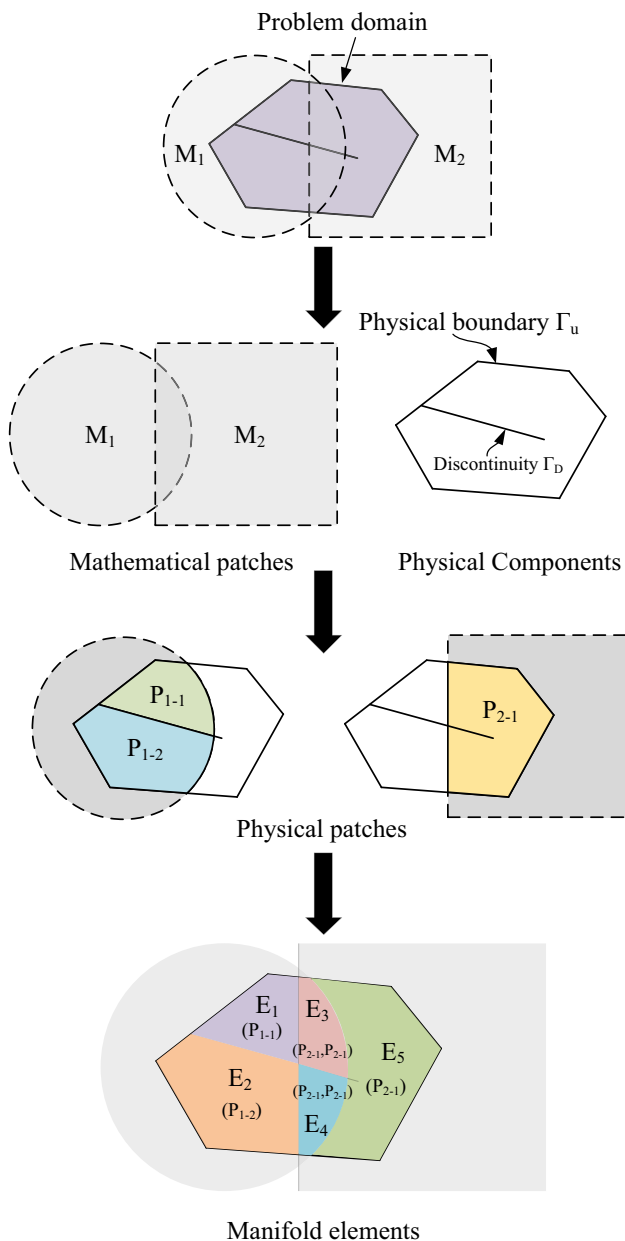


Fig. 1 Illustration of the finite cover system

To obtain the governing equations for a linear elastic problem with discontinuities, the Galerkin formulation (Lin 2003) is employed by Co-NMM. Let $u \in V$ be the displacement trial function, and $\delta u \in V_0$ be any set of admissible test functions. The weak form of the discrete problem is to find u^h in the finite-dimensional subspace $V^h \subset V$, $\forall \delta u^h \in V_0^h \subset V_0$, such that

$$\int_{\Omega^h} \sigma(u^h) \cdot \varepsilon(\delta u^h) d\Omega + \int_{\Omega^h} \rho \ddot{u}^h \cdot \delta u^h d\Omega + \lambda \int_{\Gamma_u^h} (u^h - \bar{u}) \cdot \delta u^h d\Gamma$$

$$= \int_{\Gamma_b^h} \delta u^h \cdot p d\Gamma + \int_{\Gamma_t^h} \bar{t} \cdot \delta u^h d\Gamma + \int_{\Omega^h} b \cdot \delta u^h d\Omega + \int_{\Gamma_c^h} c_f(u^h) \cdot \omega(\delta u^h) d\Gamma, \tag{5}$$

where σ and ε are the stress and strain tensors, respectively; Ω^h is the problem domain subjected to the body force b ; λ is the real penalty value; \bar{u} and \bar{t} are the displacement and traction conditions on the corresponding boundaries Γ_u^h and Γ_t^h , respectively; ρ is the material density; ω is the opening or sliding displacement of the cohesive element; c_f is the force exerted by cohesive element on the unbroken grain boundary Γ_c^h , which is computed based on a bilinear stress–displacement constitutive model introduced in Sect. 2.3; and p is the contact force on the broken grain boundary Γ_b^h , which is computed based on a grain-based contact model introduced in Sect. 2.4.

2.2 Rock Micro-structure Model Generation

In Co-NMM, the Voronoi tessellation technique (Malan and Napier 1995), which divides a domain into regions based on the distances to points in a specific subset of the domain, is first used as a pre-processor to build the rock micro-grains by random polygons. The detailed grain-based model generation procedures are illustrated in Fig. 2. The formed random polygonal blocks in Fig. 2a

are treated as the physical components and intersected with the mathematical cover in Fig. 2b to generate the manifold elements and eventually the corresponding grain-based model in Fig. 2c. Then, to more realistically and efficiently capture the interaction between the rock grains, as well as further simulate the rock fracturing process, zero-thickness cohesive elements are embedded between

two adjacent grains as shown in Fig. 3. With the grain-based model and the corresponding zero-thickness cohesive elements, modelling of the rock failure process that involves the transition from a continuum to a discontinuum through deformation, fracturing and movement can easily be achieved by considering the rock micro-structure.

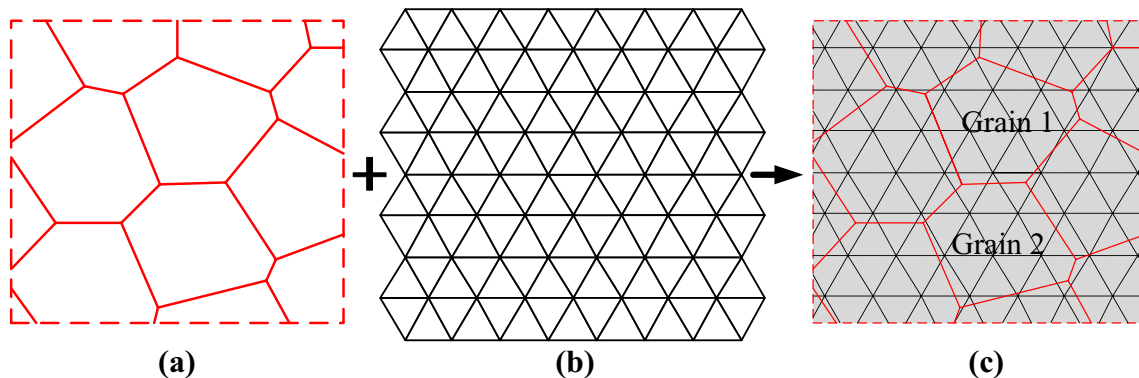


Fig. 2 Grains generation procedures. **a** Voronoi random polygonal blocks; **b** corresponding mathematical cover; **c** generated grain-based model

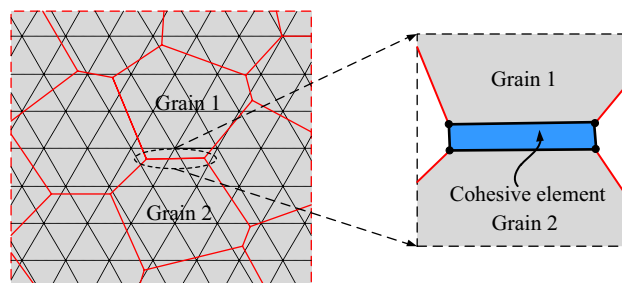


Fig. 3 Zero thickness cohesive element embedded in grain boundaries

2.3 Cohesive Fracture Model

In Co-NMM, a bilinear stress–displacement constitutive model is adopted for the zero-thickness cohesive elements, which divides the grain interactions into two types: tensile (mode-I) and shear (mode-II) behaviors. As shown in Fig. 4a, b, the tensile and shear behaviors both include two stages (hardening and softening stages), which are governed by the tensile strength f_t and mode-I fracture energy G_I (the area of the purple region in Fig. 4a) and the shear strength f_s and mode-II fracture energy G_{II} (the area of the yellow region in Fig. 4b), respectively. In the hardening stages, the tensile and shear stresses of the cohesive element both vary linearly with the opening and sliding displacements, respectively, until the strength (f_t for tensile and f_s for shear) is reached. The cohesive element will then fall into the softening stage, where the tensile and shear stresses are controlled by a damage-based softening criterion, which is expressed as follows:

$$\begin{cases} \sigma_t = (1 - D_o) \cdot f_t \\ \tau = (1 - D_s) \cdot c + \sigma_n \cdot \tan \varphi \end{cases} \quad (6)$$

where σ_t and τ are the tensile and shear stresses of the cohesive element, respectively; c is the shear cohesion; σ_n is the compressive stress; φ is the friction angle; and D_o and D_s are the mode-I and mode-II damage factors, respectively, and defined as follows:

$$\begin{cases} D_o = 0 & o < o_p \\ D_o = \frac{o - o_p}{o_r - o_p} & o_p \leq o \leq o_r \\ D_o = 1 & o > o_r \end{cases}, \begin{cases} D_s = 0 & s < s_p \\ D_s = \frac{s - s_p}{s_r - s_p} & s_p \leq s \leq s_r \\ D_s = 1 & s > s_r \end{cases} \quad (7)$$

where o_p is the critical opening corresponding to f_t ; o_r is the residual opening displacement; s_p is the critical sliding corresponding to f_s and s_r is the residual sliding displacement.

The mode-I failure of the cohesive element occurs, when D_o equals 1, and the mode-II failure takes place when D_s is equal to 1. In addition to the mode-I and mode-II failures of the cohesive element, a mixed-mode failure criterion shown in Fig. 4c is adopted to determine the mixed failure of the cohesive element, which couples the opening and sliding displacements as follows:

$$\left(\frac{o - o_p}{o_r - o_p} \right)^2 + \left(\frac{s - s_p}{s_r - s_p} \right)^2 \geq 1 \quad o_p < o < o_r \text{ and } s_p < s < s_r. \quad (8)$$

Once Eq. (8) is satisfied, a mixed-mode failure is predicted. Regardless of which failure type is predicted in the current step, the corresponding cohesive elements will be eliminated in the next calculation step.

2.4 Contact Detection and Grain Interaction After Failure

After the failure of cohesive elements, the interaction between grains is captured by the grain-based contact model instead of the corrupted cohesive elements. The basic contact elements are the grains as shown in Fig. 2c, which are taken as the closed domains encompassed by corner vertices on the boundary and detected by a contact detection algorithm at each time step to search possible contact pairs between them. There are three types of contacts between grains including angle–angle, angle–edge and edge–edge, as shown in Fig. 5. An edge–edge contact can also be transformed into two angle–edge contacts with angle V_1 to edge V_3V_4 and angle V_3 to edge V_1V_2 . After the determination of the contact type, by the relative normal displacement, w , of the contact pair and Coulomb friction law, the contact status of a contact pair can be judged, based on which the

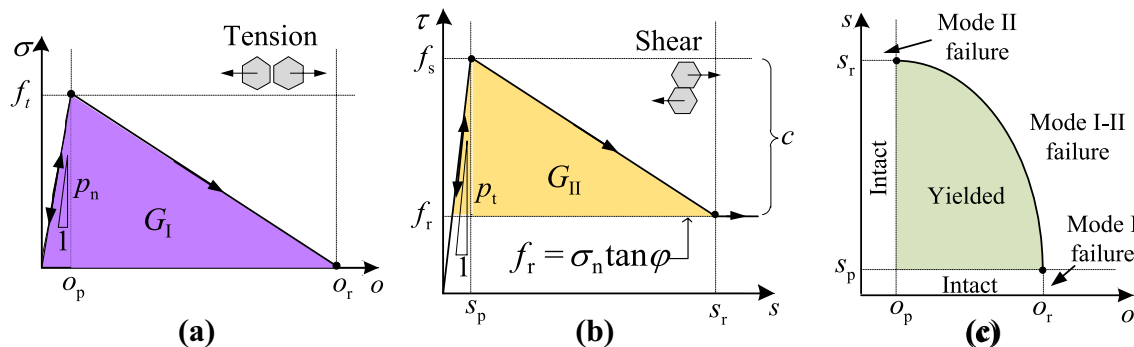


Fig. 4 Constitutive model of cohesive element; **a** mode-I tensile behavior; **b** mode-II shear behavior **c** mixed-mode failure criterion modified from (Lisjak et al. 2017) (color image online)

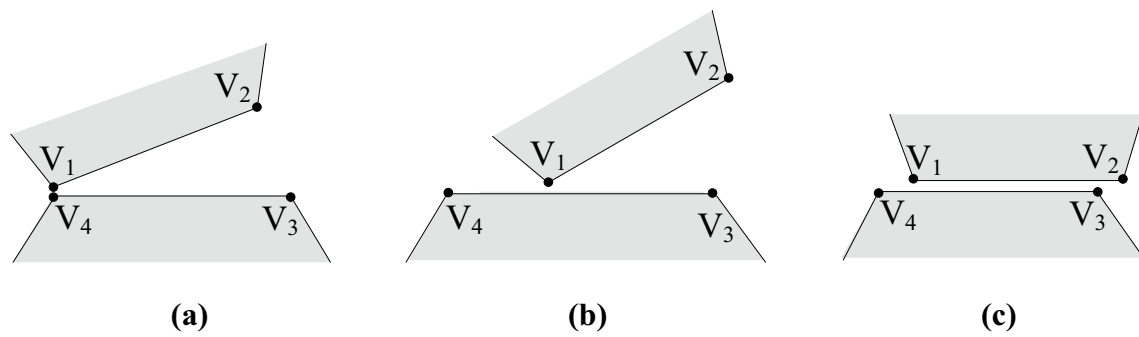


Fig. 5 Three types of grain-based contacts; **a** angle–angle; **b** angle–edge **c** edge–edge

interactive normal and tangential forces F_n and F_s , respectively, can be obtained by a force–displacement model as follows:

For the “open” state ($w > 0$), the normal and tangential forces F_n and F_s are:

$$F_n = F_s = 0, \tag{9}$$

and for the “locked” state ($w \leq 0, F_s \leq F_n \cdot \tan\varphi$), F_n and F_s are:

$$\begin{cases} F_n = k_n w \\ F_s = k_s s \end{cases}, \tag{10}$$

and for the “sliding” state ($w \leq 0, F_s > F_n \cdot \tan\varphi$), F_n and F_s are:

$$\begin{cases} F_n = k_n w \\ F_s = F_n \cdot \tan\varphi \end{cases}, \tag{11}$$

where s is the relative tangential displacement of the contact pair; k_n and k_s are the normal and tangential contact spring stiffness, respectively; φ is the friction angle of the contact interface.

3 Coupled Hydro-mechanical Formulation of Co-NMM

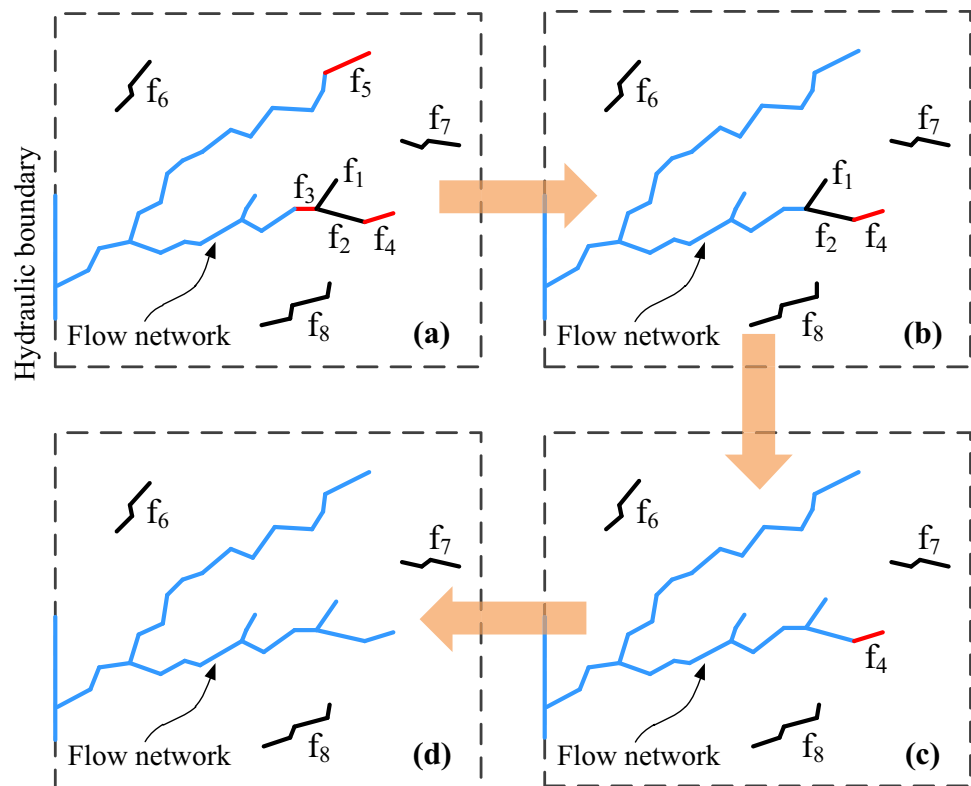
In this section, an explicit hydraulic solving framework that iteratively calculates the flow rate and fluid pressure in each time step is proposed based on the cubic law and linear compressibility model. Then, by converting the fluid pressure obtained from the hydraulic solver into nodal forces of the manifold elements, the mechanical solver (Co-NMM) is used to calculate the deformation and fracturing process of the rock, based on which the geometrical characteristics of the flow network is updated. Finally, by alternating between the hydraulic and mechanical solvers described above in

each time step, a two-way coupled hydro-mechanical method can be obtained. The implementation process of the hydraulic solving framework and the coupled HM approach are described below.

3.1 Hydraulic Solving Framework

The flow network, which consists of interconnected failed cohesive elements that link with hydraulic boundaries, is the only path for fluid flow as well as the hydraulic solving. Therefore, to calculate the flow rate and fluid pressure, a flow network searching algorithm is first proposed to initialize and update the flow network in the coupled HM process, which considers all of the failed cohesive elements, pre-existing natural fractures and hydraulic boundaries and builds the relationship between them. Before executing the searching algorithm, an initial fracture set that consists of all kinds of fractures (i.e., hydraulically induced and pre-existing natural fractures) and a flow network that consists of the hydraulic boundaries are established. The flow network searching is then conducted as follows: for each fracture in the fracture set, it is determined whether it connects to the flow network or not. If the fracture connects to the flow network, it will be eliminated from the fracture set and added into the flow network. By repeating this process until no fractures in the fracture set connect with the flow network, the flow network search in the first step is finished, and the formed flow network is then used for the flow rate and fluid pressure calculation in the next time step. In the next time step, during the mechanical analysis, the predicted failed cohesive elements are temporarily added to the fracture set. Based on the newly formed fracture set and the flow network formed in the previous time step, the flow network searching conducted in the first time step is repeated to update the fracture set and flow network for the next time step calculation. By repeating the above process until the end of the simulation, the fluid flow can be coupled to the fracture propagation. Figure 6 shows an example illustrating the flow network searching procedures in a time step, in

Fig. 6 Flow network forming procedure in each time step (color image online)



which the black lines represent the fracture set generated in the previous time steps; the red lines represent the fractures generated in the current time step; and the blue lines represent the flow network formed in the previous time step. Before the searching, a fracture set consisting of fractures from the previous fracture set and newly generated fractures (f_{1-8} shown in Fig. 6a) is first established. Then, with the first determination process, fractures f_3 and f_5 are added into the flow network as shown in Fig. 6b, and fractures f_1 and f_2 are subsequently captured by the second determination process as shown in Fig. 6c. Finally, as shown in Fig. 6d, fracture f_4 is also added into the flow network by the third judging process, and fractures $f_{6,8}$ remain in the fracture set because they are still isolated from the flow network.

To calculate the fluid pressure of the flow network obtained by the searching algorithm, the flow network is first represented by a series of virtual nodes, which correspond to the intersections of fractures in the flow network and act as fluid containers with a uniform pressure. These nodes are connected together by flow channels that are generated from interconnected failed cohesive elements and pre-existing fractures. As shown in Fig. 7a, b, the selected part of the flow network is represented by nodes 1–9, which are connected together by flow channels f_{c1-8} . A particular flow channel is the only path for fluid flow between adjacent nodes. For example, flow channel f_{c1} is the only path for fluid flow between nodes 1 and 2 as shown in Fig. 7c. The nodes act as fluid containers, which therefore have volumes. The volume of each node is assumed

to be equal to half the total volume of all of the flow channels connected to the node, which can be expressed as follows:

$$V = \sum_n \frac{V_n}{2}, \quad (12)$$

where n indexing over all flow channels connecting to the node; V is the volume of node; V_n is the volume of the flow channel and calculated as:

$$V_n = a_n \cdot L_n, \quad (13)$$

where a_n and L_n are the equivalent hydraulic aperture and length of the flow channel, respectively, as detailed below. As shown in Fig. 7d, the volume of node 7 is equal to half the total volume of flow channels f_{c6} and f_{c8} .

Due to the assumption of laminar viscous flow, the flow rate between adjacent nodes can be obtained by the cubic law which is based on the parallel plate model. However, the two walls of the flow channel are not parallel in most cases, and the hydraulic aperture may vary along the flow channel as shown in Fig. 8. To satisfy the parallel plate model, the hydraulic aperture of the flow channel must be adjusted to an equivalent aperture in advance as follows (Jing et al. 2001):

$$\begin{cases} a_m = \frac{1}{2}(a_i + a_j) \\ a = a_m \left[\frac{16r^2}{(1+r)^4} \right]^{1/3}, \end{cases} \quad (14)$$

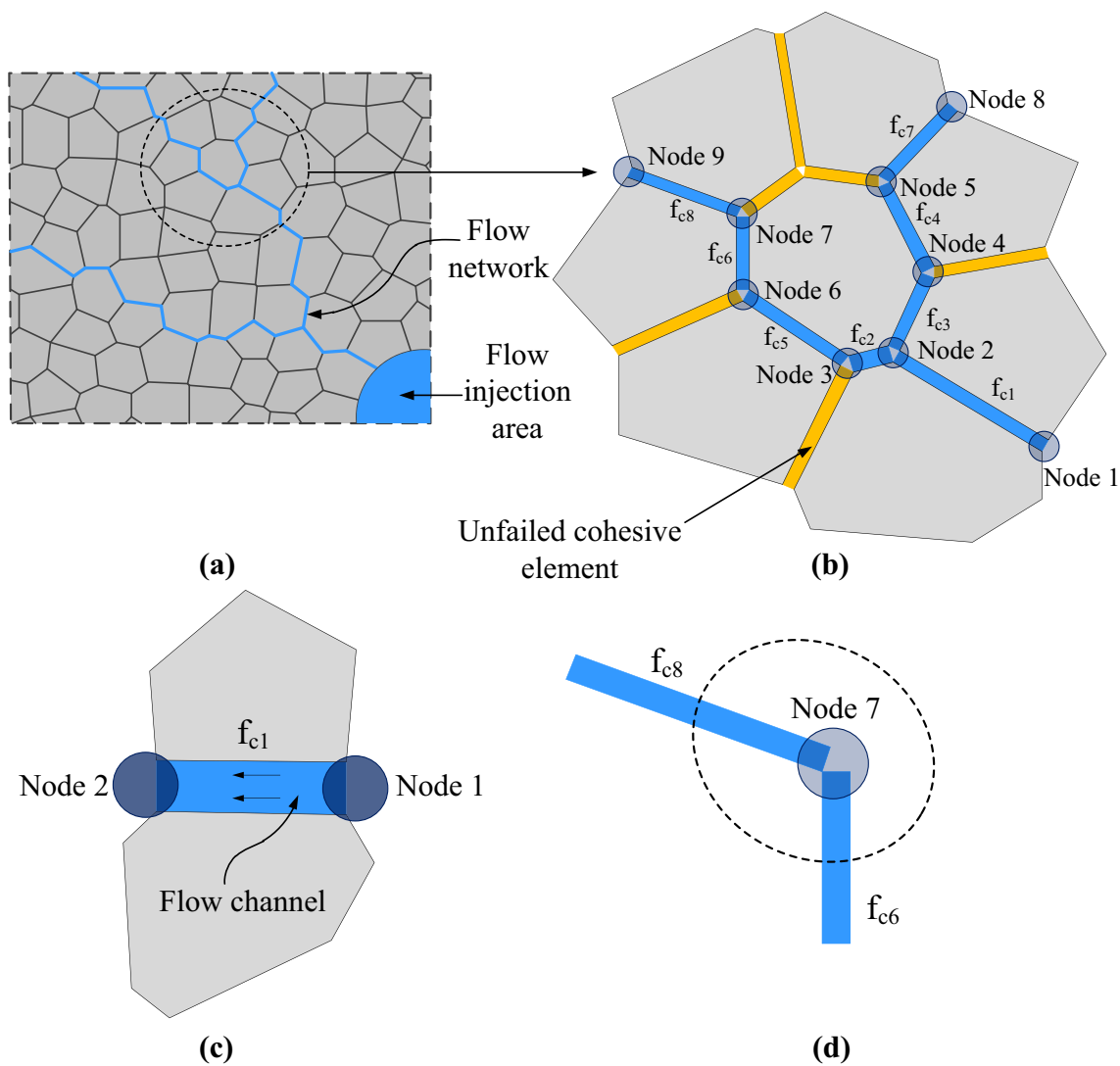


Fig. 7 Hydraulic solving model; **a** problem analysis model; **b** nodes and flow channels generated from flow network; **c** fluid flow between adjacent nodes; **d** the volume of node (color image online)

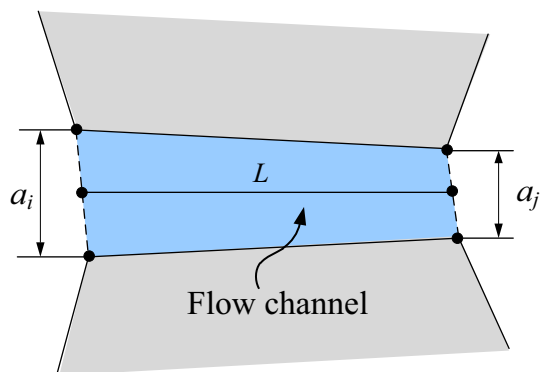


Fig. 8 Flow channel with linearly varying hydraulic aperture

where a_i and a_j are the hydraulic apertures at the two ends of the flow channel; a_m is a mean hydraulic aperture; $r = a_j/a_i$; a is an equivalent hydraulic aperture. Then by this rectification, a non-parallel flow channel can be treated as a parallel flow channel with an equivalent aperture.

Based on the assumptions described above, the flow rate from node i to j can be calculated by the cubic law as:

$$q_{ij} = -\frac{a^3 \Delta p_{ij}}{12\mu L}, \tag{15}$$

where μ is the dynamic viscosity of the fluid, L is the length of the flow channel connecting nodes i and j ; and $\Delta p_{ij} = p_j - p_i + \rho_f g(y_j - y_i)$ is the pressure differential between nodes i and j , where p_i and p_j are the fluid pressures inside nodes i and j , respectively; ρ_f is the fluid density; g is the

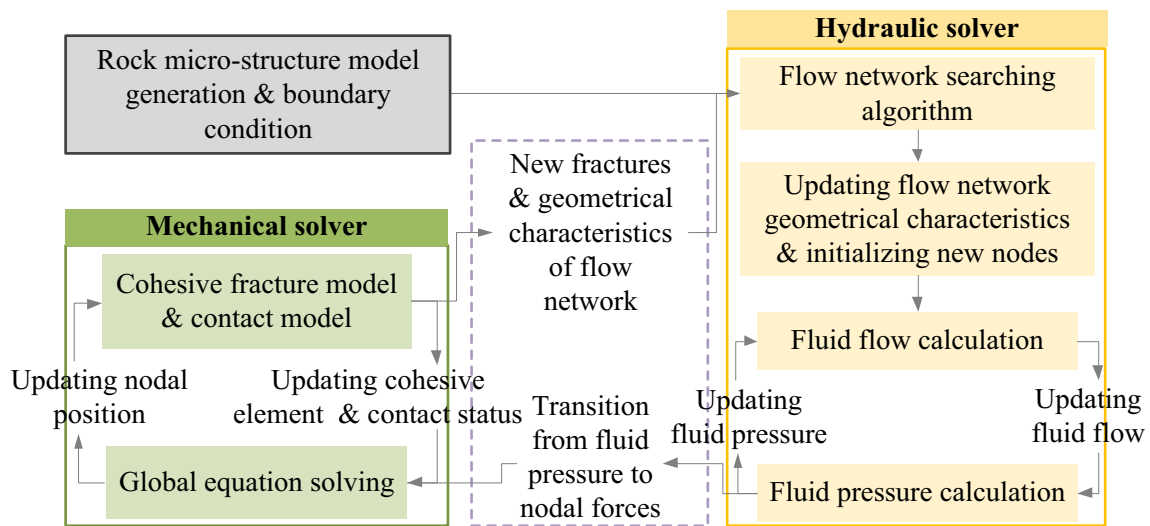


Fig. 9 HM coupling procedures

acceleration of gravity; and y_j and y_i are the elevations at the two ends of the flow channel, respectively.

As shown in Eq. (15), under the effect of gravity, fluid flow can occur between two nodes that are not fully saturated. In this case, the permeability of the flow channel should actually decrease as the saturation decreases; however, this is not considered by Eq. (15). To solve this inconsistency for Eq. (15), a dimensionless coefficient f_s , which depends on the saturation of the node from which inflow occurs, is incorporated into Eq. (15) to account for the effect of saturation on the permeability of the flow channel as follows (Itasca 2005):

$$\begin{cases} q_{ij} = -\frac{a^3 \Delta p_{ij}}{12\mu L} \cdot f_s \\ f_s = S_i^2(3 - 2S_i) \\ S_i = \frac{V_f}{V_i} \end{cases}, \quad (16)$$

where S_i is the saturation of node i ; V_f is the volume of fluid inside node i ; and V_i is the volume of node i . It should be noted that if the calculated value of S_i is greater than 1, S_i should be reassigned to be 1.

Then, by summing all of the flow rates in the flow channels connected to node i , the total inflow rate of node i can be expressed as:

$$Q_i = \sum_j q_{ji}, \quad (17)$$

with j indexing over all of the nodes adjacent to node i .

Finally, based on the total inflow rate and the volume change of the node induced by the mechanical response, a linear compressibility model (Itasca 2005; Lisjak et al. 2017) is adopted to calculate the fluid pressure acting on each node as follows:

$$P^t = \begin{cases} P^{t-1} + K_f \frac{Q^t \Delta t}{V^t} - K_f \frac{V^t - V^{t-1}}{(V^t + V^{t-1})/2} S^t = 1, \\ 0 \quad 0 \leq S^t < 1 \end{cases}, \quad (18)$$

where P^t and P^{t-1} are the fluid pressures of the node at time steps t and $t - 1$, respectively; K_f is the bulk modulus of the fluid; V^t and V^{t-1} are the volumes of the node at time steps t and $t - 1$, respectively; Q^t and S^t are the total inflow rate and the saturation of the node at time step t , respectively; and Δt is the time step size.

To guarantee the computational convergence of the explicit hydraulic solving process, a threshold value for the time step size should be set as (Itasca 2005; Lisjak et al. 2017)

$$\Delta t^* = \min_i \left(\frac{V_i}{\frac{K_f}{12\mu} \sum_j \frac{a_j^3}{L_j}} \right), \quad (19)$$

with i and j indexing over all of the nodes and the flow channels connected to each node, respectively. It should be noted that the temporal threshold should be updated in each time step due to the change in the geometrical characteristics of the flow network, such as the hydraulic aperture.

3.2 Coupled Hydro-mechanical Approach

To extend the Co-NMM for coupled HM analysis, a fully coupled HM formulation is implemented by alternating between the implicit mechanical solver (Co-NMM) and the explicit hydraulic solver in each time step. As shown in Fig. 9, the rock micro-structure model is first established, which is represented by rock grains and cohesive elements. According to the rock micro-structure model and boundary conditions, the flow network is initially determined for the first time step and will be continuously updated by the flow network searching algorithm at the beginning of each time step based on the mechanical analysis results of the last step. With the searched flow network, the cubic law and linear fluid compressibility model are then successively adopted to calculate the flow rate and fluid pressure of the flow network at each time step. The calculated fluid pressure of the flow network is then taken as an external linearly distributed load acting on the boundaries of the grains (flow channels) and later further transformed into nodal forces of the manifold elements. With these nodal forces, the mechanical analysis is performed by the Co-NMM, based on which the nodal positions as well as the status of the cohesive elements and contacts between grains are updated at the end of each time step. The updated nodal positions and the newly failed cohesive elements are later used in the next step to update the flow network as well as the flow network geometrical characteristics for the hydraulic solving. By repeating the above coupled HM procedures between the mechanical and hydraulic solvers in each time step until the end of the simulation, a fully coupled HM analysis by Co-NMM is achieved.

4 Numerical Validation

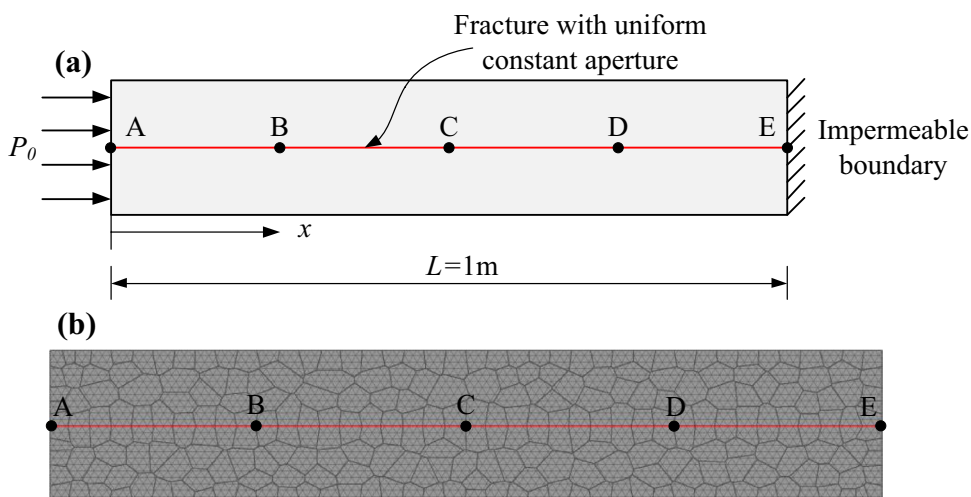
This section presents four validation examples for the developed coupled HM scheme against analytical solutions and experiment results, including two coupled and two uncoupled examples. The proposed hydraulic solving framework is first verified with the two uncoupled examples, which analyse transient and steady flows through fractures with constant and uniform apertures. Then, two coupled examples, which respectively consider the elastic response of a pressurized fracture and hydraulic fracture propagation under different perforation inclinations and in situ stresses, are adopted to validate the coupled HM approach. The four validation examples are described below.

4.1 Transient Flow in a Single Fracture

In this example, transient flow through a single fracture is studied. As shown in Fig. 10a, a fracture with a constant and uniform aperture of $a = 3 \times 10^{-5}$ m and a length of $L = 1$ m is horizontally embedded in the centre of the model. Points A–E are five measurement points that are evenly distributed along the fracture. The fracture is assumed to be originally dry and impermeable at the right boundary and then suddenly subjected to a constant fluid pressure, $P_0 = 9.5$ MPa, at the left side. Based on the above assumptions, transient flow will occur from left to right in the fracture, which can be modelled by a 1-D heat conduction equation (Carslaw and Jaeger 1959) that is expressed as:

$$P = P_0 \cdot \left\{ 1 + \frac{4}{\pi} \sum_{n=0}^{\infty} \left[e^{-(2n+1)^2(T/4)\pi^2} \cdot \cos\left(\frac{(2n+1)\pi}{2}\zeta\right) \cdot \left(\frac{(-1)^{n+1}}{2n+1}\right) \right] \right\}, \tag{20}$$

Fig. 10 Modelling transient flow in a single fracture **a** model geometry and boundary conditions modified from (Lisjak et al. 2017); **b** the numerical model



where $\zeta = (L - x)/L$; and T is dimensionless time, which is computed as:

$$T = \frac{K_f(a^2/12\mu)t}{L^2} \tag{21}$$

In the example, the bulk modulus K_f and dynamic viscosity μ of the fluid are adopted as 2.2 GPa and 10^{-3} Pa s, respectively. To model the example, a numerical model containing 6027 physical patches, 278 grains and 7885 manifold elements as shown in Fig. 10b is constructed, in which the fracture is discretized into 40 equal length flow channels. The evolution of the fluid pressure is recorded at each node along the fracture.

The simulated fluid pressure distributions along the fracture at four time points and the temporal evolution of the fluid pressure at points A–E are respectively compared with the corresponding analytical results obtained by Eq. (20) as shown in Fig. 11. The numerical results agree well with the analytical solutions, which demonstrates that the proposed model can successfully model transient flow through a fracture with a constant and uniform aperture.

4.2 Fracture Seepage with a Free Surface

As shown in Fig. 12a, this example studies 2-D seepage through a homogeneous aquifer. The homogeneous aquifer with dimensions of $4\text{ m} \times 8\text{ m}$ has an impermeable bottom boundary, and two constant hydraulic heads $h_1 = 4\text{ m}$ and $h_2 = 1\text{ m}$ are imposed on the left and right boundaries, respectively. According to Dupuit’s formula (Harr 1962), when the fluid flow reaches a steady state, the position of the free surface $h(x)$ and the total discharge Q can be obtained by:

$$h(x) = \sqrt{h_1^2 - \frac{h_1^2 - h_2^2}{L}x}, \tag{22}$$

and

$$Q = k \frac{h_1^2 - h_2^2}{2L}, \tag{23}$$

respectively, where L is the length of the model; and k is the intrinsic hydraulic conductivity.

To model this example, a numerical model containing 25,966 physical patches, 2449 rock grains and 28,620 manifold elements is established, as shown in Fig. 12b, which is discretized by two sets of parallel fractures with a constant and uniform aperture, $a = 10^{-4}\text{ m}$; and constant fracture spacing, $S = 0.5\text{ m}$. The system of two sets of parallel fractures is the flow network, which is further subdivided by the Voronoi polygonal mesh. The calculation parameters are as follows: $K_f = 2.2\text{ GPa}$, $\mu = 10^{-3}\text{ Pa s}$, $\rho_f = 1000\text{ kg/m}^3$, and

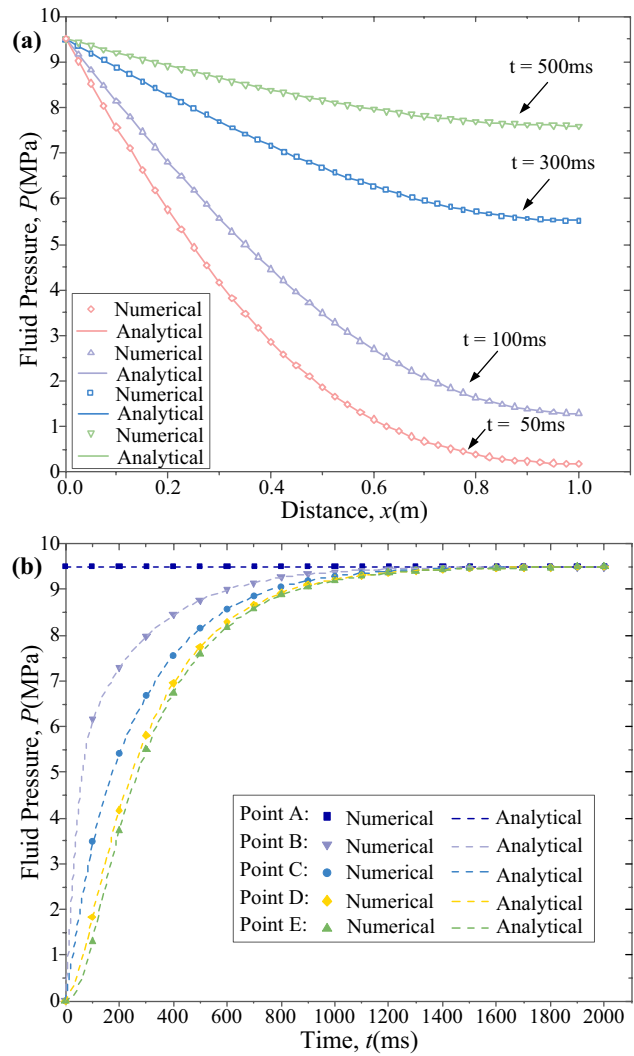


Fig. 11 **a** Comparison between analytical and numerical fluid pressure distribution at four different moments inside the fracture; **b** comparison between analytical and numerical evolution of fluid pressure at five equipartition points along the fracture

$g = 10\text{ m/s}^2$. The intrinsic hydraulic conductivity k can be computed by (Wu and Wong 2014):

$$k = \frac{\rho_f g a^3}{12\mu S}, \tag{24}$$

which is equal to $1.666 \times 10^{-6}\text{ m/s}$ here.

According to Eq. (23), the total discharge is $1.562 \times 10^{-6}\text{ m}^3/\text{s}$. By summing all of the discharges of the nodes on the right boundary, the computed numerical total discharge is $1.641 \times 10^{-6}\text{ m}^3/\text{s}$, which agrees well with the analytical solution with only a 5.1% deviation.

To further illustrate the accuracy of the developed model, the numerically predicted steady-state position of the free surface is compared with that of the analytical solution obtained by Eq. (22) as shown in Fig. 13. The steady-state

Fig. 12 Modelling seepage in a homogeneous aquifer; **a** model geometry and boundary conditions; **b** the numerical model

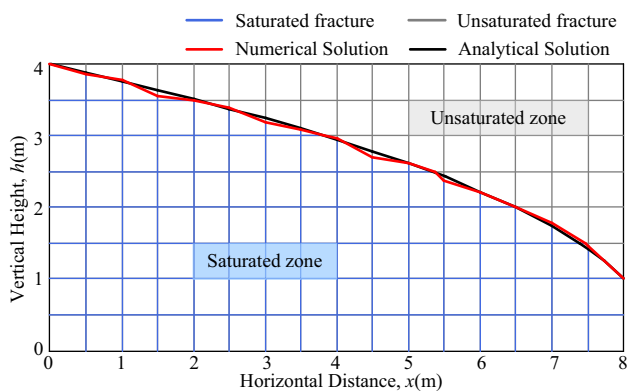
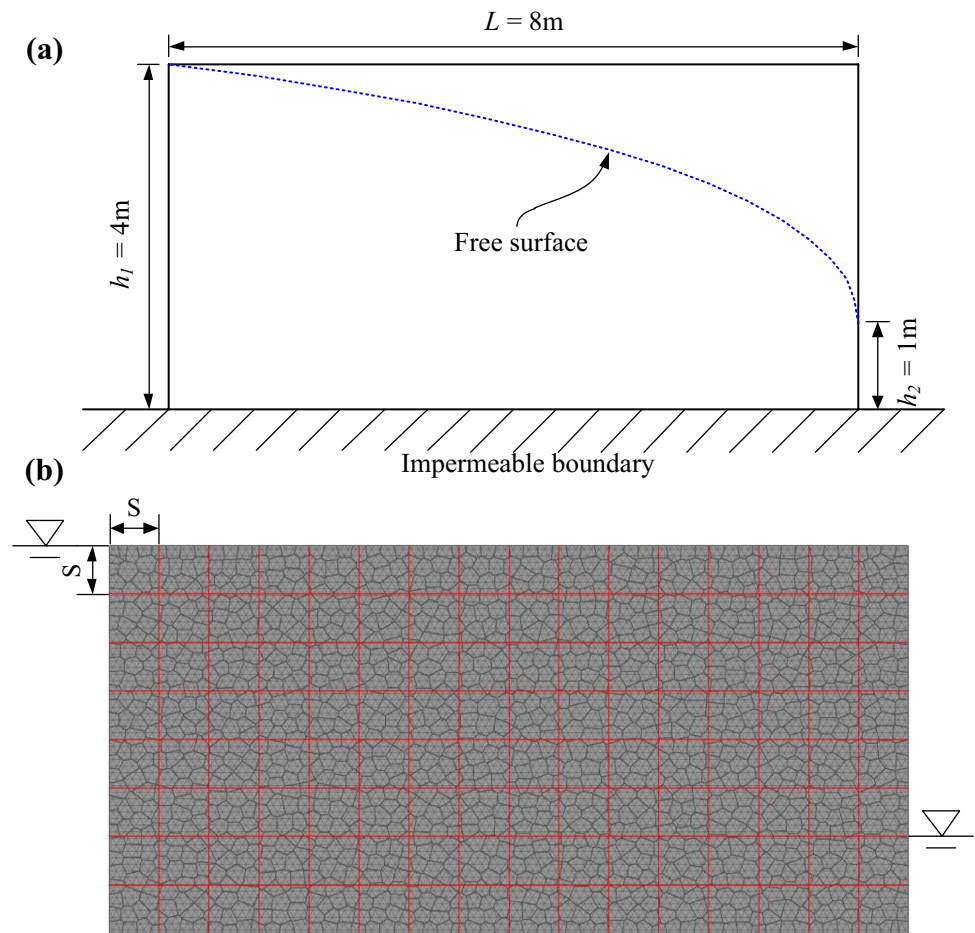


Fig. 13 The comparison between numerical and analytical solutions for the position of free surface (color image online)

free surface is the boundary between the saturated and unsaturated zones. Therefore, to obtain the numerical steady-state position of the free surface, the neighboring nodes at the boundary between the saturated and unsaturated zones are connected with straight line segments to form the continuous free surface shown by the red line in Fig. 13. As shown in Fig. 13, the numerically predicted free surface generally

agrees well with the analytical result despite the slight misfit caused by the relatively coarse grain size used in the modelling, which can be alleviated by adopting a finer grain model. The comparisons shown in Figs. 12 and 13 indicate that the steady flow through fractures with a constant and uniform aperture can be well captured by the proposed model.

4.3 Fluid-Pressurized Fracture Embedded in an Elastic Rock Matrix

In this example, the elastic response of a fluid-pressurized fracture is presented. As shown in Fig. 14a, a fracture with a length of 21.6 m is horizontally embedded in the centre of a linear elastic rock mass with dimensions of 46.08 m × 46.08 m and subjected to a uniform fluid pressure, $P = 20$ MPa, along its two walls. In situ principal stresses $\sigma_v = -15$ MPa and $\sigma_h = -30$ MPa are imposed on the model in the vertical and horizontal directions, respectively. The Young's modulus E and Poisson's ratio ν of the rock mass are set to 40 GPa and 0.22, respectively. To prevent rock failure and keep the model in the elastic stage, high strength properties are assigned to the cohesive elements; for example, the normal and tangential penalty

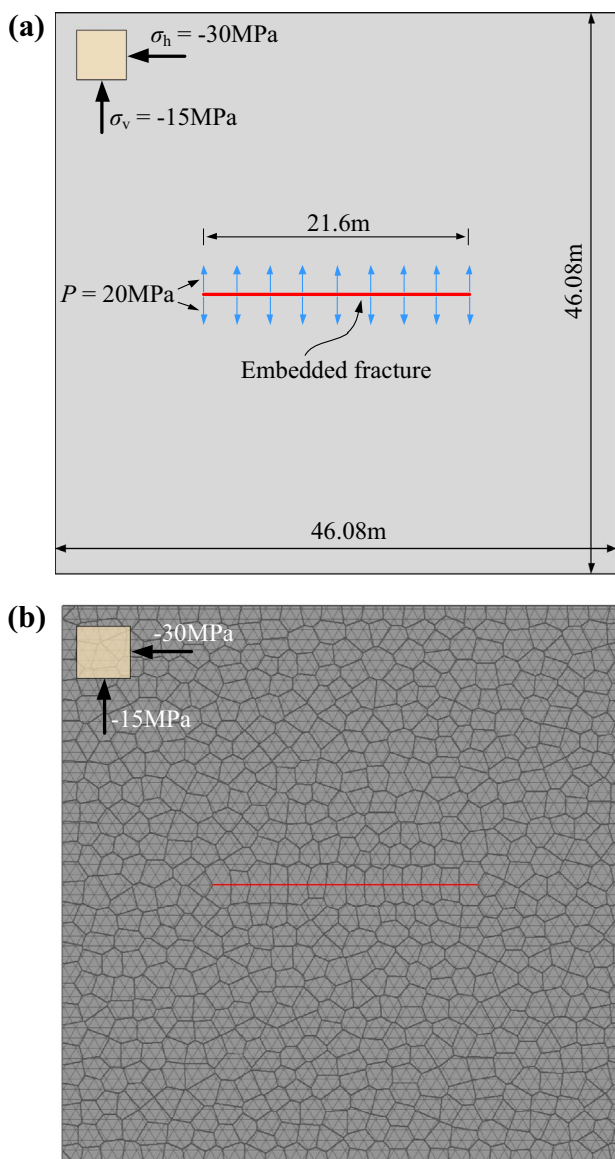


Fig. 14 Modelling pressurized fracture embedded in elastic rock matrix; **a** model geometry and boundary conditions; **b** the numerical model

parameters are both ten times the Young’s modulus (Itasca 2005). The analytical solution for the hydraulic aperture along the fracture can be expressed as follows (Parker 1981):

$$a(x) = \frac{4(\sigma_v + P)(1 - \nu^2)}{E} \sqrt{L^2 - x^2}, \tag{25}$$

where L is half the length of the fracture; x is the distance from the fracture centre and $a(x)$ is the hydraulic aperture at x .

To model the example as shown in Fig. 14b, a numerical model containing 9291 physical patches, 680 grains and

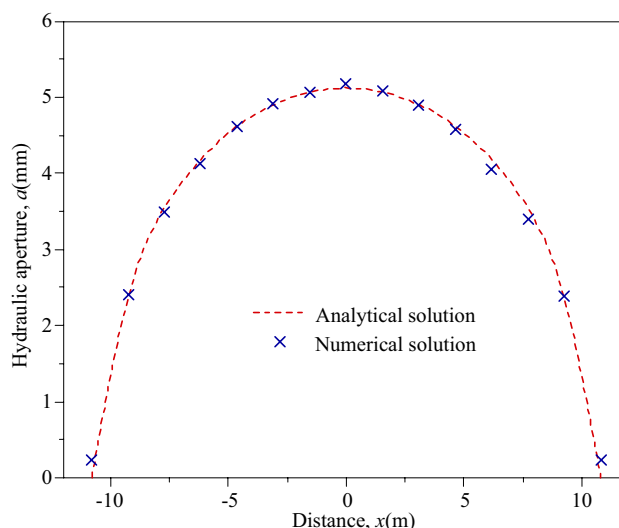


Fig. 15 Comparison between analytical and numerical hydraulic aperture distribution along the fracture

10,878 manifold elements is constructed. In the numerical model, the embedded fracture is discretized into 14 flow channels, based on which the fluid pressure is applied and the hydraulic aperture along the fracture is captured. As shown in Fig. 15, the numerical solution for the hydraulic aperture distribution along the fracture is compared with the analytical solution given by Eq. (25), in which the numerical solution is presented by a series of points representing the hydraulic apertures at nodes along the fracture, and the analytical solution is shown by a dashed line. The comparison shows that the numerical solution is in good agreement with the analytical solution, which demonstrates that the proposed model can well capture the coupled HM elastic response of a fractured rock mass subjected to hydraulic pressure.

4.4 Hydraulic Fracturing Through Oriented Perforations

Oriented perforation fracturing technology, which perforates wellbores to form the favorable fluid passageways between the wellbore and the reservoir, is widely used for hydraulic fracturing treatments. In this example, the effects of the perforation inclination and in situ stress on hydraulic fracture propagation with oriented perforations, which have been experimentally studied in detail by Chen et al. (2010), are numerically investigated to validate the proposed model in modelling the coupled HM failure process. As shown in Fig. 16a, a wellbore with a diameter of 20 mm is placed in the centre of the model and connected to two symmetrical perforations with lengths of 30 mm. The micro-mechanical parameters adopted in this section are calibrated based on

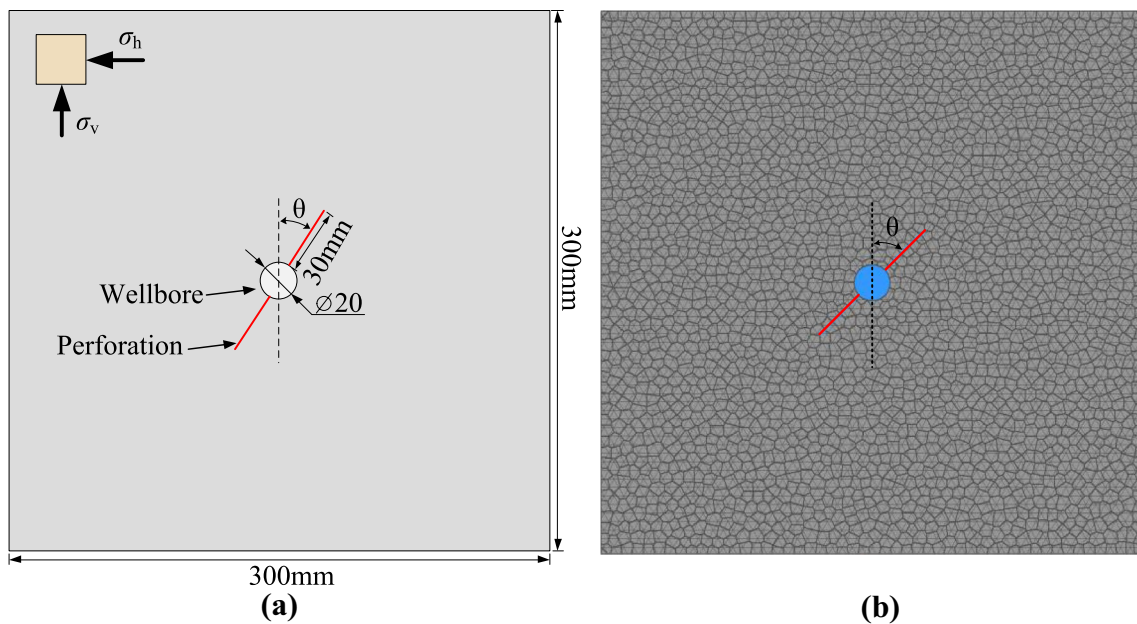


Fig. 16 Modelling hydraulic fracturing through oriented perforations; **a** model geometry and boundary conditions; **b** the numerical model

Table 1 Mechanical and hydraulic parameters for concrete samples

Parameters	Value
Grains	
Bulk density, ρ (kg/m ³)	2300
Young's modulus, E (GPa)	8.402
Poisson's ratio, ν	0.23
Grain size (mean), (mm)	5
Cohesive element	
Tensile strength, f_t (MPa)	1.8
Internal cohesion, c (MPa)	9.0
Friction angle of intact material, φ_c (°)	35
Mode I fracture energy, G_I (J/m ²)	11.9
Mode II fracture energy, G_{II} (J/m ²)	47.6
Normal penalty parameters, p_{fn} (GPa)	84
Tangential penalty parameters, p_{ft} (GPa)	8.5
Hydraulic parameter	
Bulk modulus of fluid, K_f (GPa)	2.2
Dynamic viscosity, μ (mPa s)	133
Density of fluid, ρ_f (kg/m ³)	1000
Contact interaction parameter	
Normal contact penalty, p_n (GPa)	84
Tangential contact penalty, p_t (GPa/m)	33.6
Friction angle of fractures, φ_f (°)	35

the macro-mechanical properties of a concrete sample from Chen et al. (2010) and reported in Table 1. An initial integration time step of 1×10^{-6} s is employed, which is continuously adjusted according to the latest temporal threshold

obtained by Eq. (19) in each time step. The fluid injection rate is kept at 0.35 MPa/ms until the wellbore pressure reaches 10 MPa. The other hydraulic parameters are also listed in Table 1.

To investigate the effect of the in situ stress on hydraulic fracture propagation with oriented perforations, four in situ stress states are considered, while the perforation inclination θ is set to be 45° clockwise from the direction of the maximum compressive in situ stress σ_v . The simulated hydraulic fracture pattern and corresponding maximum principal stress (tension is positive) evolution process during fracture propagation for each in situ stresses condition are shown in Figs. 17, 18, 19, 20 and 21.

As shown in Fig. 17a, when the in situ stress is hydrostatic, the hydraulic fractures initiate from the tips of the perforation and propagate approximately in the direction of the perforation, which can be explained by the corresponding maximum principal stress evolution contours shown in Fig. 18. As shown in Fig. 18a, before fracture initiation, tensile stress concentrations are located at the perforation tips. Then with the propagation of the hydraulic fracture, as shown in Fig. 18b–d, the fracture tips always move along with the regions of concentrated tension stresses that develop ahead of the fracture tips in the direction of the perforations in this case.

In the second case as shown in Fig. 17b, when the difference in the in situ stresses increases to 3 MPa, the hydraulic fractures also initiate from the tips of the perforations but, gradually deviate away from the direction of the perforation to the direction of the maximum compressive in situ stress

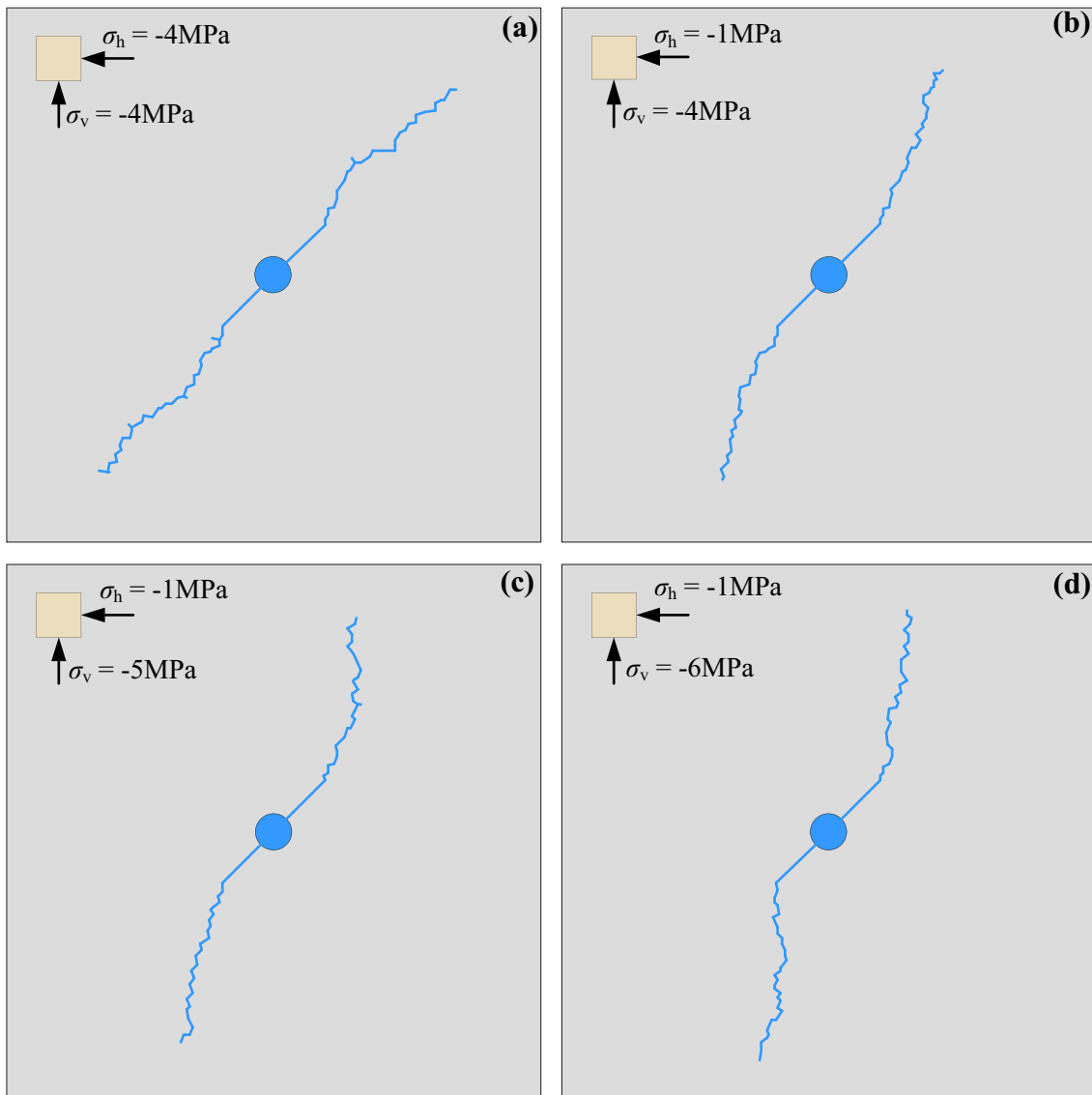


Fig. 17 Hydraulic fracture patterns for different in situ stresses; **a** case 1: $\sigma_v = -4$ MPa and $\sigma_h = -4$ MPa; **b** case 2: $\sigma_v = -4$ MPa and $\sigma_h = -1$ MPa; **c** case 3: $\sigma_v = -5$ MPa and $\sigma_h = -1$ MPa **d** case 4: $\sigma_v = -6$ MPa and $\sigma_h = -1$ MPa

σ_v . The corresponding maximum principal stress evolution contours shown in Fig. 19 indicate that before fracture initiation, tensile stress concentration are located at the perforation tips as well as the upper left and lower right of the wellbore, and the tensile stresses at the perforation tips are much larger than those at the upper left and lower right of the wellbore (Fig. 19a). Then, as shown in Fig. 19b–d, as the fracture propagates, the fracture tips move along with the regions of concentrated tension stresses and gradually deviate towards the direction of the maximum compressive in situ stress σ_v . This phenomenon is caused by the gradual deviation of the direction of the maximum principal stress at the fracture tips towards the direction of σ_v .

Similar to case 2, in cases 3 and 4 respectively shown in Fig. 17c, d, the hydraulic fractures also initiate from the tips of the perforations. However, with increasing difference in the in situ stresses (from 3 MPa in case 2 to 5 MPa in case 4), the propagation of the hydraulic fractures to the direction of the maximum compressive in situ stress σ_v becomes faster and faster. As shown in Figs. 20 and 21, the evolutions of the maximum principal stress for cases 3 and 4 are similar to that described in case 2 (Fig. 19); however, with increasing difference in the in situ stresses, the time required for the direction of the maximum principal stresses at the fracture tips to deviate towards the direction of σ_v decreases. These results demonstrate that the larger the difference in the in situ stresses is, the faster the hydraulic fractures

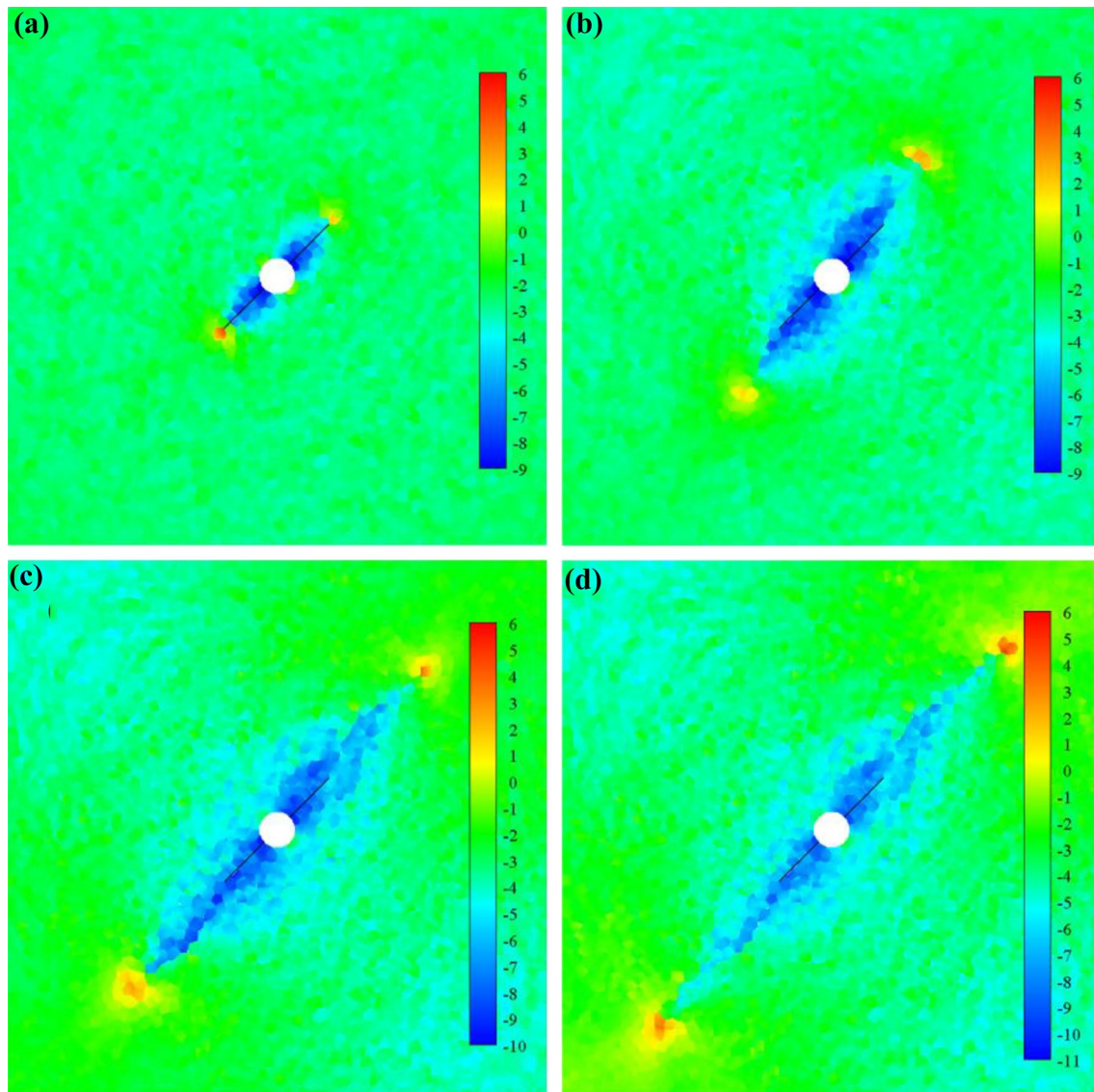


Fig. 18 Maximum principal stress evolution contours for in situ stresses $\sigma_v = -4$ MPa and $\sigma_h = -4$ MPa; **a** step 30,000; **b** step 60,000; **c** step 102,000; **d** step 132,000 (color image online)

reorient towards the direction of the maximum compressive in situ stress σ_v , which is generally consistent with the experimental results obtained by Chen et al. (2010).

With four different perforation inclinations oriented 15° , 30° , 45° and 60° clockwise from the direction of the maximum compressive in situ stress σ_v , the effect of the perforation inclination on hydraulic fracture propagation is studied. The in situ stresses σ_v and σ_h are set at -5 MPa and -1 MPa, respectively. The simulated hydraulic fracture patterns for each perforation inclination condition are respectively presented in Fig. 22a–d. The results show that the hydraulic fractures all initiate from the tips of the perforations and gradually propagate from the direction of the perforation to the direction of the maximum compressive

in situ stress σ_v , and each case has two reorientation radii corresponding to the two generated hydraulic fractures. The reorientation radius is defined as the distance between the centre of the wellbore and the fracture tip when the hydraulic fracture has just conspicuously turned to the direction of the maximum compressive in situ stress σ_v (Chen et al. 2010). By averaging the two reorientation radii in each case, the mean reorientation radii in each case are obtained as 48.65 mm, 77.75 mm, 87.8 mm and 98.4 mm, respectively. The above results suggest that with increasing perforation inclination, the hydraulic fracture requires a longer reorientation radius to turn to the direction of the maximum compressive in situ stress σ_v , which is generally consistent with the experimental results obtained by Chen et al. (2010).

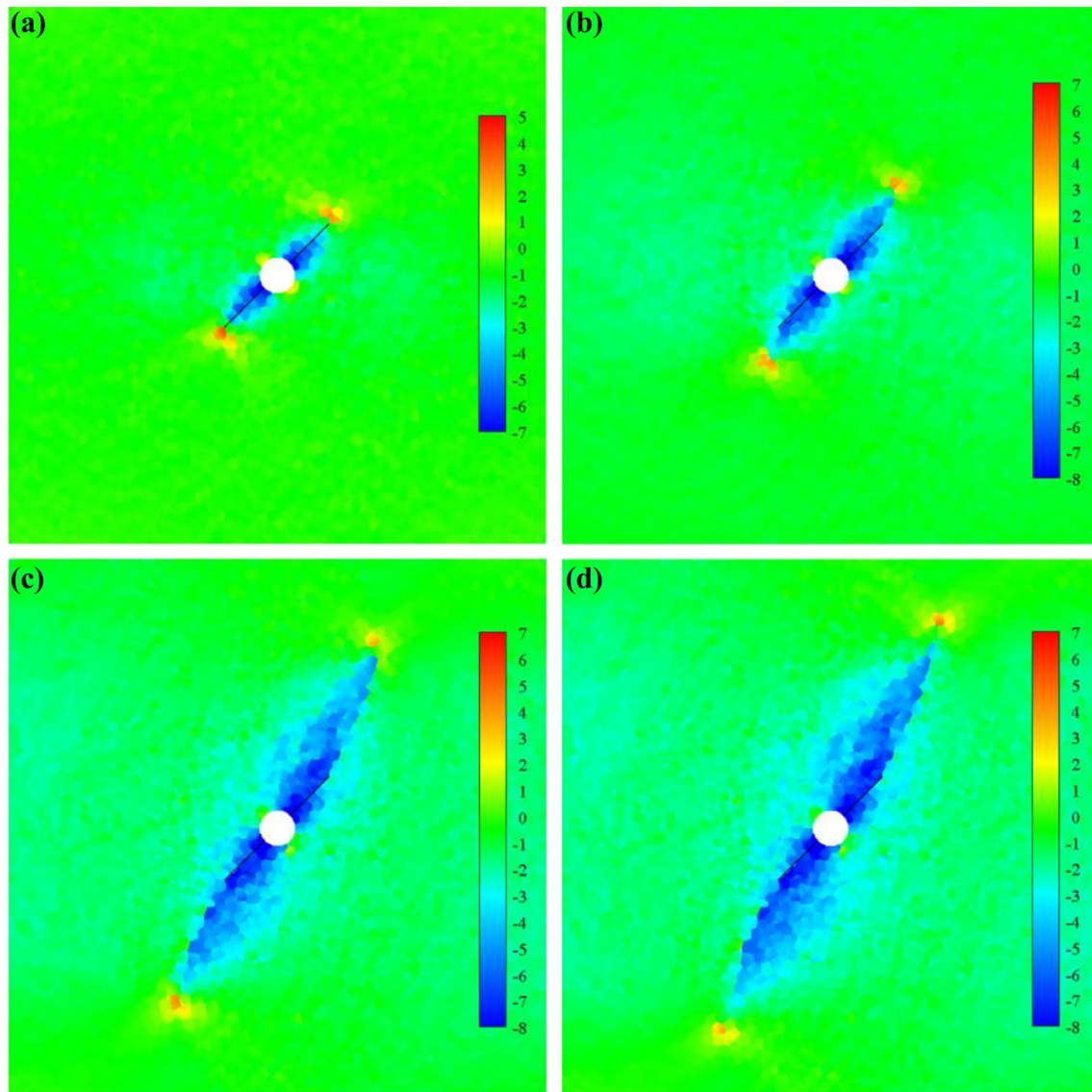


Fig. 19 Maximum principal stress evolution contours for in situ stresses $\sigma_v = -4$ MPa and $\sigma_h = -1$ MPa; **a** step 27,000; **b** step 39,000; **c** step 63,000; **d** step 75,000 (color image online)

Based on the two groups of comparisons presented above, good agreement between the numerical and experimental results is achieved, which demonstrates that the proposed model can satisfactorily capture the coupled HM failure process.

5 Application to Micro-scale Hydraulic Fracturing Modelling

The proposed coupled HM method is further applied to investigate the effect of the friction coefficient of natural fractures (NFs) on hydraulic fracture (HF) propagation in Augig granite (AG), which is a coarse-grained crystalline

rock composed of mineral grains ranging from 2 to 6 mm (average of 4 mm). As shown in Fig. 23a, the model with the dimensions of 200 mm \times 300 mm is subjected to in situ stresses $\sigma_h = -10$ MPa and $\sigma_v = -2$ MPa in the horizontal and vertical directions, respectively. An injection wellbore with a diameter of 20 mm is placed in the centre of the model. Four parallel NFs, which are denoted N_1 , N_2 , N_3 and N_4 from left to right, are embedded at an inclination angle of 60° in the model and, are centrosymmetrically distributed along the centre of the injection wellbore. The coordinates of the upper and lower tips of the NFs N_1 – N_4 are shown in Fig. 23a. Based on the mean mineral grain size presented above, the numerical model in Fig. 23b is discretized into 3570 grains with a mean size of 4 mm. The model contains

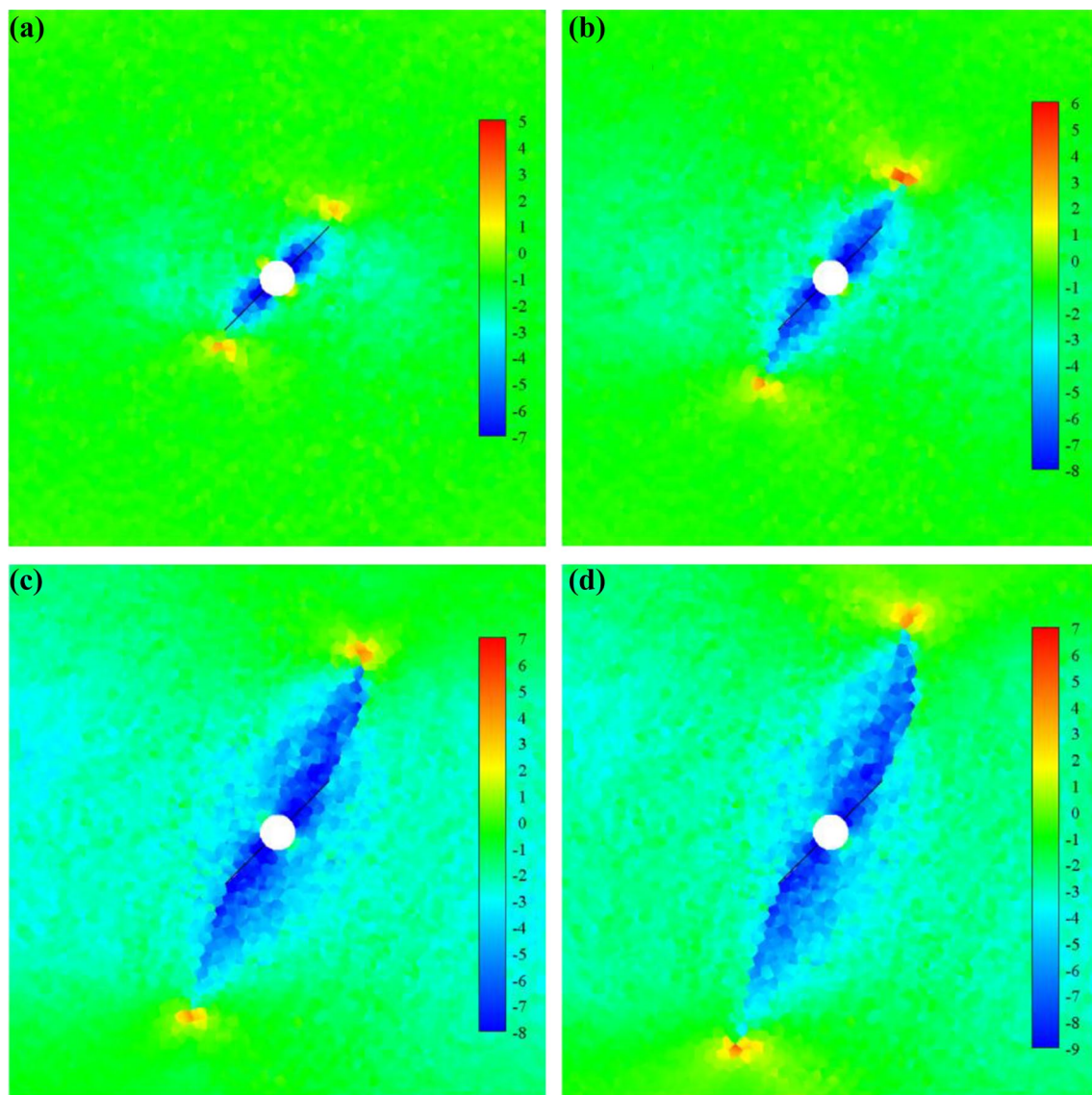


Fig. 20 Maximum principal stress evolution contours for in situ stresses $\sigma_v = -5$ MPa and $\sigma_h = -1$ MPa; **a** step 24,000; **b** step 33,000; **c** step 51,000; **d** step 72,000 (color image online)

37,373 physical patches and 40,325 manifold elements. The mechanical micro-parameters used in this model are calibrated by Wu et al. (2018) based on the macro-mechanical properties of AG obtained from laboratory tests (Table 2). The NFs are modelled by interconnecting weaker cohesive elements, the strength parameters of which are ten times weaker than those of the cohesive elements in intact rock. An initial integration time step of 1×10^{-7} s is adopted. The injection rate is kept constant at 0.5 MPa/ms until the wellbore pressure reaches 15 MPa. The other hydraulic parameters are listed in Table 2.

To investigate the effect of the friction coefficient of NFs on HF propagation, four friction coefficients (0.4, 0.6, 0.8 and 1.0) are assigned to the NFs shown in Fig. 23. As shown

in Figs. 24, 25, 26 and 27, for these four models with different NF friction coefficients, four HF patterns with different scenarios of interaction between the HF and NFs as well as different failure modes are captured. In Figs. 24, 25, 26 and 27, the grey lines represent NFs, the green lines represent HF with tensile failures, the red lines represent HF with shear failures and the blue lines represent HF with mixed failures.

As illustrated in these figures, for all four cases, before intersecting with the NFs, the HF all initiate from the wall of the wellbore and propagate approximately in the direction of the maximum compressive in situ stress σ_h . These HF consist of a series of inter-granular fractures induced by tensile and mixed failures. However, when

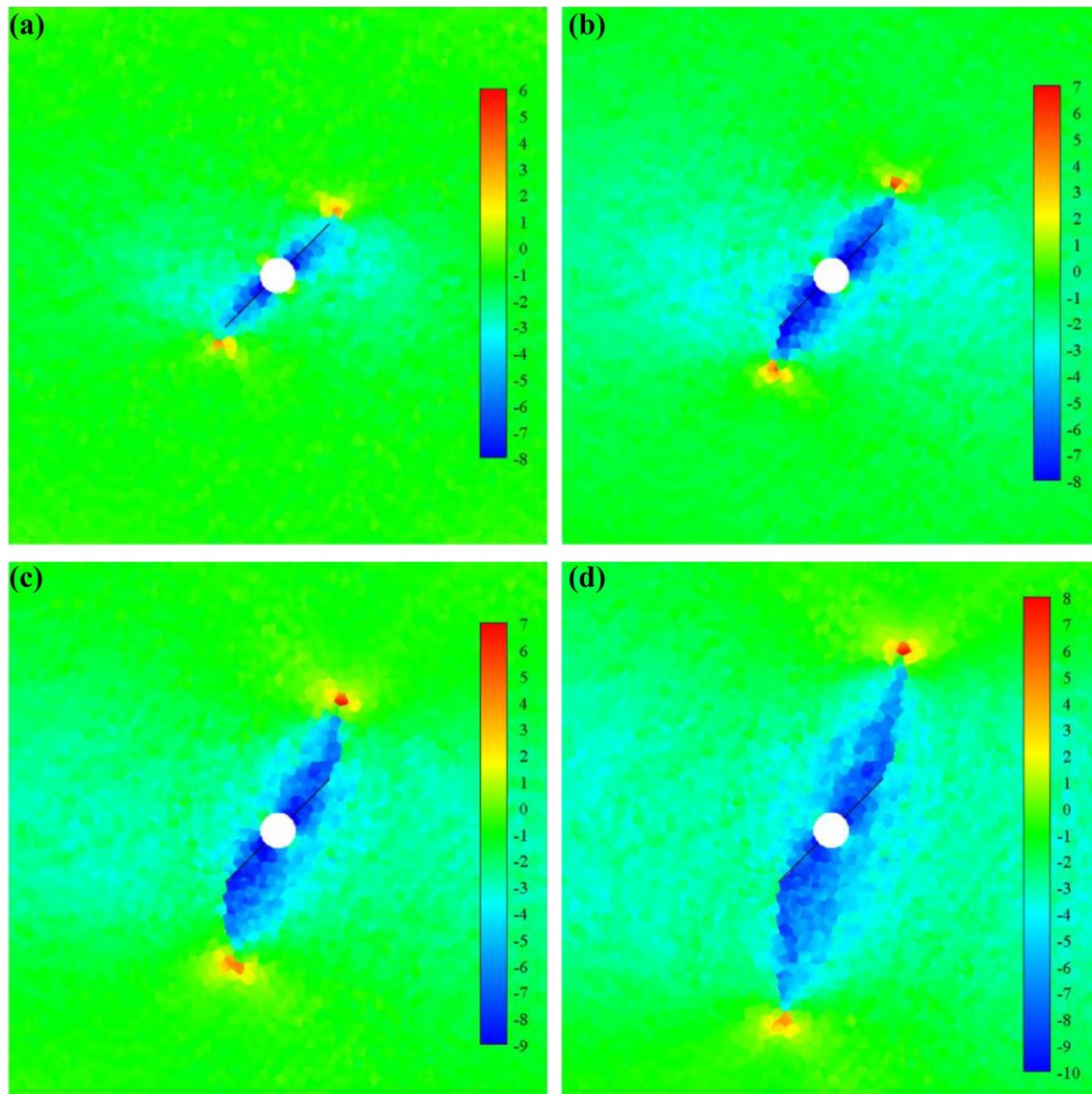


Fig. 21 Maximum principal stress evolution contours for in situ stresses $\sigma_v = -6$ MPa and $\sigma_h = -1$ MPa; **a** step 27,000; **b** step 36,000; **c** step 48,000; **d** step 66,000 (color image online)

encountering the NFs, the HFs in case 1 (friction coefficient 0.4) (Fig. 24) are respectively arrested by N_2 and N_3 . Since the friction of the NFs is low in this case, both N_2 and N_3 fail in a shear dominated mode (with minor mixed-mode failure). As a result, with the fluid flow, the generated HFs initially tend to propagate along N_2 and N_3 and then re-initiate at the lower tip of N_2 and the upper tip of N_3 due to the local tensile stress concentrations. As the injection continues, the HFs continue to propagate in the direction of the maximum compressive in situ stress σ_h due to a series of tensile failures induced by the fluid pressure. Upon further propagation, the tensile HFs are respectively arrested by N_1 and N_4 . Due to the low friction of the NFs, the lower part of N_1 and the upper part of N_4 both fail in

the shear mode. Finally, after propagating along N_1 and N_4 , the HFs re-initiate respectively at the lower tip of N_1 and the upper tip of N_4 due to the local tensile stress concentrations. The above results reveal that the failure of NFs is dominated by the shear mode, which is attributed to the low friction coefficient of the NFs.

When the NF friction coefficient increases to 0.6 in case 2, as shown in Fig. 25, the HFs are sequentially arrested by the four NFs, which is similar to the result of case 1. The lower part of N_2 and the upper part of N_3 both fail in the shear dominated mode (with minor mixed-mode failure), and the lower part of N_1 and the upper part of N_4 both fail in the shear mode. However, due to the increase in the friction of the NFs, N_2 and N_3 are not entirely activated.

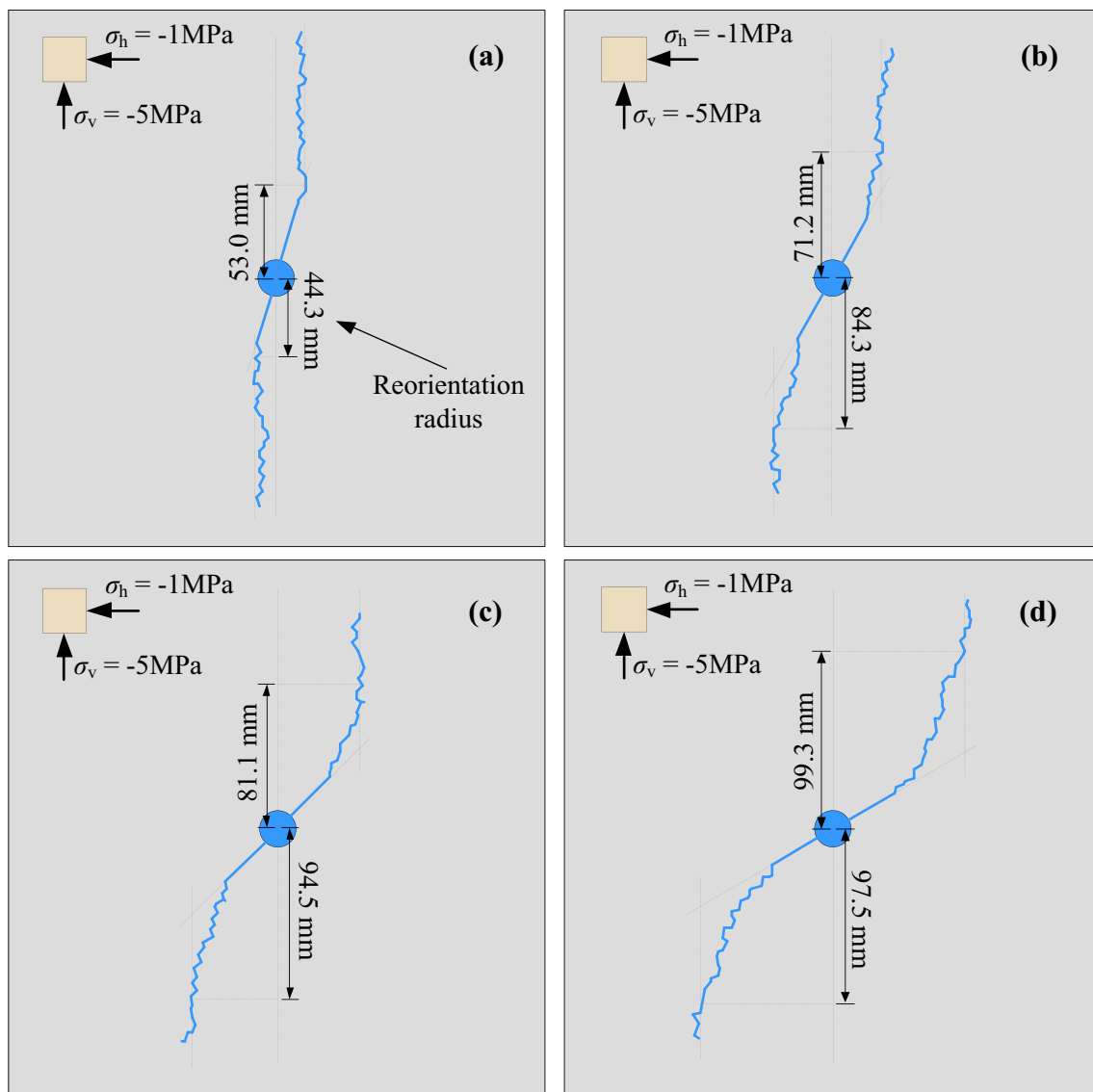


Fig. 22 Hydraulic fracture patterns for different perforation inclination; **a** $\theta = 15^\circ$; **b** $\theta = 30^\circ$; **c** $\theta = 45^\circ$; **d** $\theta = 60^\circ$

In addition, a tensile micro-fracture branch is induced near the intersection point of N_3 and the HF.

As the NF friction coefficient increases further to 0.8 in case 3, as shown in Fig. 26, the first generated HFs cross N_2 and N_3 with small offsets. As the injection continues, two small segments of mixed failure develop at the intersections of the HFs and N_2 and N_3 respectively due to the relatively high friction of the NFs. The HFs continue to propagate in the direction of the maximum compressive in situ stress σ_h , and are later arrested by N_1 and N_4 . With further fluid injection, N_1 and N_4 both fail in the shear dominated mode, accompanying with three tensile micro-fracture branches generated along N_4 and one micro-fracture branch formed at N_1 when the HFs propagate along N_1 and N_4 . Finally, the lower tip of N_1 and the

upper tip of N_4 are both re-activated via the initiation of local tensile fractures.

As shown in Fig. 27, when the NF friction coefficient increases to 1.0, the developed HFs always propagate in the direction of the maximum compressive in situ stress σ_h and mainly consist of a series of tensile fractures (with very few mixed-mode fractures). The HFs cross N_2 , N_3 and N_4 with small offsets, and an HF crosses N_1 without any offset. Since the friction of the NFs is high, unlike the previous three cases, no HF is arrested by an NF in this case. In particular, the generated HFs first cross N_2 and N_3 with small offsets in mixed failure modes. However, due to the high friction of the NFs, the two mixed failures are respectively confined to the intersections of the HFs and N_2 and N_3 . With further fluid injection, the HFs continue to propagate in the direction of

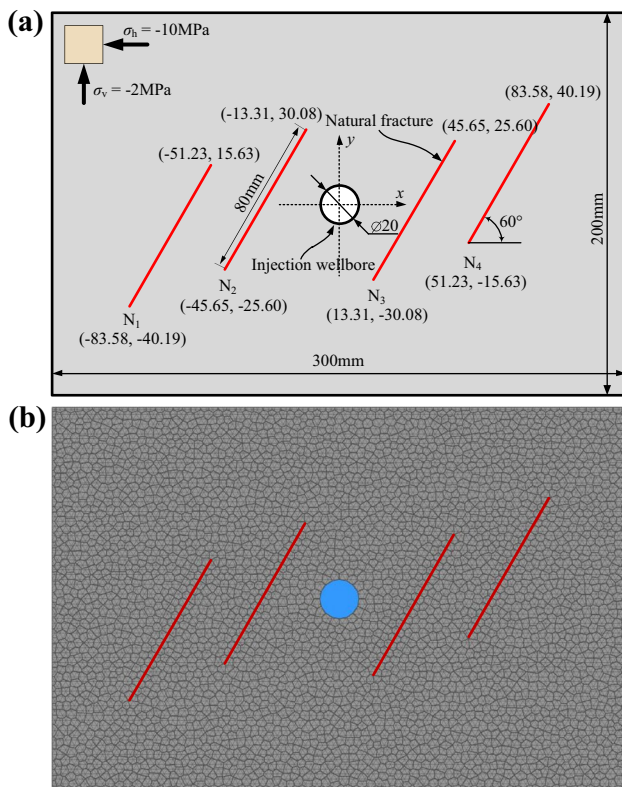


Fig. 23 Modelling micro-scale hydraulic fracturing in Augig granite; **a** model geometry and boundary conditions; **b** the numerical model

the maximum compressive in situ stress σ_h until intersecting with N_1 and N_4 . Then, the HF directly crosses N_1 without inducing any failure, which simply divides N_1 into two parts. Meanwhile, the HF crosses N_4 with a small offset due to the mixed failure along N_4 . The results of case 4 clearly show that the type of interaction between the HFs and NFs is dominated by a small offset crossing or direct crossing, which indicates that it is difficult for the NFs with a high friction coefficient to fail.

The four cases presented above (Figs. 24, 25, 26, 27) elucidate that most of the failures of the NFs are in the shear mode. With an increase in the friction coefficient of the NFs (from 0.4 to 1.0), it becomes more difficult for the NFs to fail, which results in simpler failure patterns due to the change in the interaction type between the HFs and NFs, i.e., from HFs being arrested by NFs to HFs crossing the NFs with an offset and then to HFs directly crossing the NFs.

6 Conclusions

The key merit of this paper is the development of a fully coupled HM formulation based on Co-NMM for modelling hydraulic fracturing at micro-scale. The cubic law and a linear fluid compressibility model are employed by

Table 2 Mechanical and hydraulic parameters for Augig granite

Parameters	Value
Grains	
Bulk density, ρ (kg/m ³)	2600
Young's modulus, E (GPa)	25.8
Poisson's ratio, ν	0.23
Grain size (mean), (mm)	4
Cohesive element	
Tensile strength, f_t (MPa)	6.12
Internal cohesion, c (MPa)	14.7
Friction angle of intact material, φ_c (°)	30
Mode I fracture energy, G_I (J/m ²)	87.2
Mode II fracture energy, G_{II} (J/m ²)	348.8
Normal penalty parameters, p_{fn} (GPa)	650
Tangential penalty parameters, p_{ft} (GPa)	66
Natural fracture parameter	
Tensile strength, f_t^* (MPa)	0.612
Internal cohesion, c^* (MPa)	1.47
Mode I fracture energy, G_I^* (J/m ²)	8.72
Mode II fracture energy, G_{II}^* (J/m ²)	34.88
Hydraulic parameter	
Bulk modulus of fluid, K_f (GPa)	2.2
Dynamic viscosity, μ (Pa s)	0.001
Density of fluid, ρ_f (kg/m ³)	1000
Contact interaction parameter	
Normal contact penalty, p_n (GPa)	650
Tangential contact penalty, p_t (GPa)	260
Friction angle of fractures, φ_f (°)	30

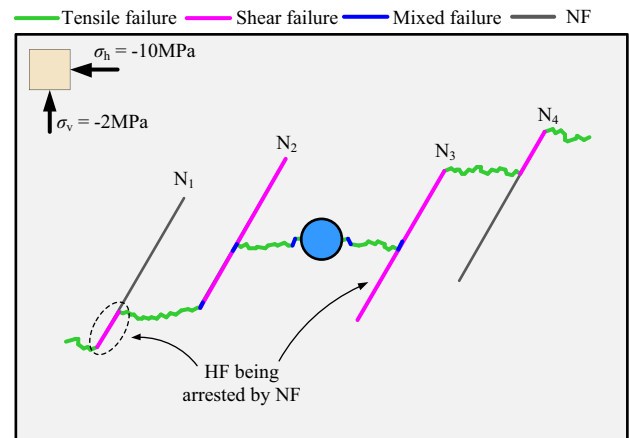


Fig. 24 Case 1: hydraulic fracture patterns for NF friction coefficient of 0.4 (color image online)

the hydraulic solver to explicitly calculate the flow rate and fluid pressure, respectively. By alternating between the implicit mechanical solver (Co-NMM) and the explicit hydraulic solver in each time step, the fully coupled

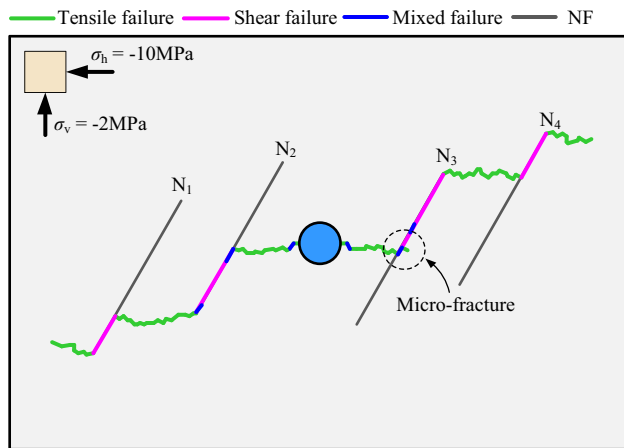


Fig. 25 Case 2: hydraulic fracture patterns for NF friction coefficient of 0.6 (color image online)

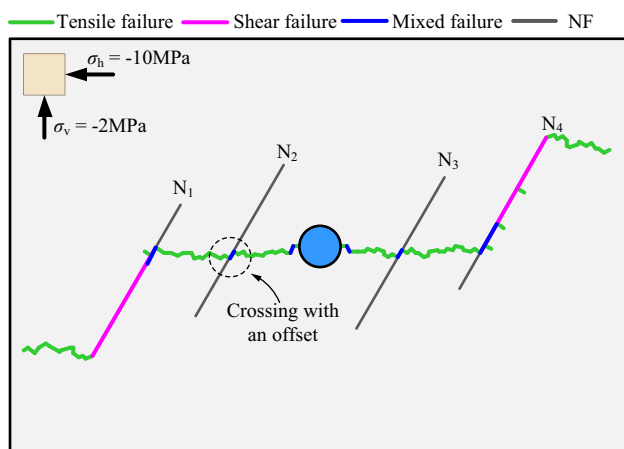


Fig. 26 Case 3: hydraulic fracture patterns for NF friction coefficient of 0.8 (color image online)

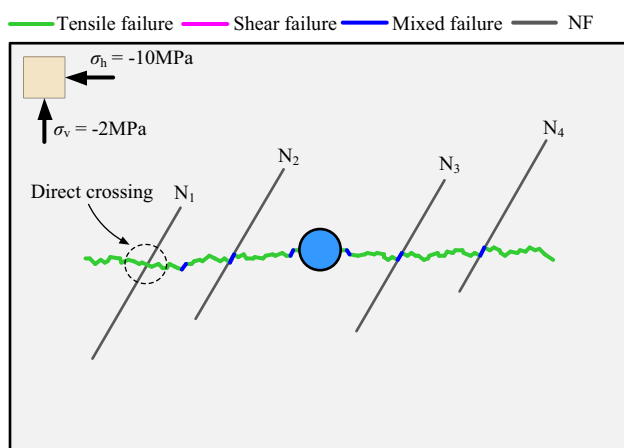


Fig. 27 Case 4: hydraulic fracture patterns for NF friction coefficient of 1.0 (color image online)

method is implemented. The capability of the developed method for modelling hydraulic fracturing is validated by a series of examples against analytical solutions as well as experiment results. Finally, the hydraulic fracture propagation processes are analysed at micro-scale in Augig granite to investigate the effect of the friction coefficient of the NFs on hydraulic fracture propagation. Based on the results from the validation and application examples, the following conclusions can be drawn:

- Based on the cubic law, the linear fluid compressibility model as well as the flow network searching algorithm, the hydraulic solver can satisfactorily capture the transient and steady flows in the continually updated fracture network.
- By alternating between the implicit mechanical solver (Co-NMM) and the explicit hydraulic solver with the time step, the developed method can well predict the elastic response of fluid-pressurized fractures and the process of hydraulic fracture propagation.
- For hydraulic fracturing through oriented perforations, with an increase in the difference between the in situ stresses, the hydraulic fracture will reorient itself towards the maximum compressive in situ stress direction more quickly. In addition, under a particular in situ stresses state, the greater the perforation inclination is, the longer the reorientation radius that is needed for the hydraulic fracture to turn to the direction of the maximum compressive in situ stress.
- For hydraulic fracturing of Augig granite (AG) possessing multi-fractures, with an increase in the friction coefficient of the NFs, it becomes more difficult for the NFs to fail, which results in simpler HF patterns. This phenomenon is associated with the change of the interaction type between HFs and NFs, i.e., from HFs being arrested by NFs to HFs crossing the NFs with an offset and then to HFs directly crossing the NFs.

The developed method has shown promise in modelling hydraulic fracturing at micro-scale. However, due to the complex characteristics of rock micro-structures and the interactions between rock micro-structures, the fracturing fluid as well as the HFs and NFs involved in modelling hydraulic fracturing at micro-scale, the cohesive fracture model of Co-NMM and coupled HM approach in this study should be further enhanced to target more realistic hydraulic fracturing modelling at micro-scale.

Acknowledgements The research work is supported by the National Natural Science Foundation of China (Grant nos. 41502283, 41772309) and the Sino-British Fellowship Trust Visitorship of the University of Hong Kong.

References

- Bai M, Roegiers J-C, Elsworth D (1995) Poromechanical response of fractured-porous rock masses. *J Petrol Sci Eng* 13:155–168
- Belytschko T, Black T (1999) Elastic crack growth in finite elements with minimal remeshing. *Int J Numer Methods Eng* 45:601–620
- Biot M, Willis D (1957) The theory of consolidation. *J Appl Elastic Coeff Mech* 24:594–601
- Carslaw H, Jaeger J (1959) *Conduction of heat in solids*, 2nd edn. Oxford University Press, Oxford
- Chen M, Jiang H, Zhang GQ, Jin Y (2010) The experimental investigation of fracture propagation behavior and fracture geometry in hydraulic fracturing through oriented perforations. *Pet Sci Technol* 28:1297–1306
- Chen W, Konietzky H, Liu C, Tan X (2018) Hydraulic fracturing simulation for heterogeneous granite by discrete element method. *Comput Geotech* 95:1–15
- Cheng W, Wang R, Jiang G, Xie J (2017) Modelling hydraulic fracturing in a complex-fracture-network reservoir with the DDM and graph theory. *J Nat Gas Sci Eng* 47:73–82
- Choo LQ, Zhao Z, Chen H, Tian Q (2016) Hydraulic fracturing modeling using the discontinuous deformation analysis (DDA) method. *Comput Geotech* 76:12–22
- Damjanac B, Cundall P (2016) Application of distinct element methods to simulation of hydraulic fracturing in naturally fractured reservoirs. *Comput Geotech* 71:283–294
- Detournay E, Cheng AH-D (1988) Poroelastic response of a borehole in a non-hydrostatic stress field. *Int J Rock Mech Min Sci Geomech Abstr* 25:171–182
- Geertsma J, de Klerck F (1969) A rapid method of predicting width and extent of hydraulically induced fractures. *J Petrol Technol* 21:1571–1581
- Goodman R (1976) *Methods of geological engineering in discontinuous rocks*
- Harr ME (1962) *Groundwater and seepage*. McGraw-Hill Book Co., Inc., New York
- Hu Y, Chen G, Cheng W, Yang Z (2014) Simulation of hydraulic fracturing in rock mass using a smeared crack model. *Comput Struct* 137:72–77
- Hu M, Rutqvist J, Wang Y (2017a) A numerical manifold method model for analyzing fully coupled hydro-mechanical processes in porous rock masses with discrete fractures. *Adv Water Resour* 102:111–126
- Hu MS, Wang Y, Rutqvist J (2017b) Fully coupled hydro-mechanical numerical manifold modeling of porous rock with dominant fractures. *Acta Geotech* 12:231–252
- Itasca (2005) UDEC version 4.0 user's manuals. Itasca Consulting Group Inc, Minnesota
- Jiao Y-Y, Zhang H-Q, Zhang X-L, Li H-B, Jiang Q-H (2015a) A two-dimensional coupled hydromechanical discontinuum model for simulating rock hydraulic fracturing. *Int J Numer Anal Methods Geomech* 39:457–481
- Jiao YY, Zhang XL, Zhang HQ, Li HB, Yang SQ, Li JC (2015b) A coupled thermo-mechanical discontinuum model for simulating rock cracking induced by temperature stresses. *Comput Geotech* 67:142–149
- Jing L, Ma Y, Fang Z (2001) Modeling of fluid flow and solid deformation for fractured rocks with discontinuous deformation analysis (DDA) method. *Int J Rock Mech Min Sci* 38:343–355
- Khrstianovic S, Zheltov Y (1955) Formation of vertical fractures by means of highly viscous liquid. Paper presented at the 4th World petroleum congress, Rome, Italy
- Li Y, Deng JG, Liu W, Feng Y (2017) Modeling hydraulic fracture propagation using cohesive zone model equipped with frictional contact capability. *Comput Geotech* 91:58–70
- Li X, Zhang QB, Li JC, Zhao J (2018) A numerical study of rock scratch tests using the particle-based numerical manifold method. *Tunn Undergr Sp Technol* 78:106–114
- Lin JS (2003) A mesh-based partition of unity method for discontinuity modeling. *Comput Methods Appl Mech Eng* 192:1515–1532
- Lisjak A, Liu Q, Zhao Q, Mahabadi OK, Grasselli G (2013) Numerical simulation of acoustic emission in brittle rocks by two-dimensional finite-discrete element analysis. *Geophys J Int* 195:423–443
- Lisjak A, Kaifosh P, He L, Tatone BSA, Mahabadi OK, Grasselli G (2017) A 2D, fully-coupled, hydro-mechanical, FDEM formulation for modelling fracturing processes in discontinuous, porous rock masses. *Comput Geotech* 81:1–18
- Ma GW, An XM, Zhang HH, Li LX (2009) Modeling complex crack problems using the numerical manifold method. *Int J Fract* 156:21–35
- Ma G, An X, He LEI (2010) The numerical manifold method: a review. *Int J Comput Methods* 07:1–32
- Mahabadi OK, Lisjak A, Munjiza A, Grasselli G (2012) Y-Geo: new combined finite-discrete element numerical code for geomechanical applications. *Int J Geomech* 12:676–688
- Malan D, Napier J (1995) Computer modeling of granular material microfracturing. *Tectonophysics* 248:21–37
- Morgan WE, Aral MM (2015) An implicitly coupled hydro-geomechanical model for hydraulic fracture simulation with the discontinuous deformation analysis. *Int J Rock Mech Min Sci* 73:82–94
- Ning YJ, Zhao ZY (2013) A detailed investigation of block dynamic sliding by the discontinuous deformation analysis. *Int J Numer Anal Methods Geomech* 37:2373–2393
- Ning YJ, Yang Z, Wei B, Gu B (2017) Advances in two-dimensional discontinuous deformation analysis for rock-mass dynamics. *Int J Geomech* 17:E6016001
- Nordgren R (1972) Propagation of vertical hydraulic fracture. *Soc Petrol Eng J* 12:306–314
- Parker AP (1981) *Mechanics of fracture and fatigue: an introduction*. E & FN Spon, London
- Perkins T, Kern L (1961) Widths of hydraulic fractures. *J Petrol Technol* 13:937–949
- Rabczuk T, Belytschko T (2004) Cracking particles: a simplified mesh-free method for arbitrary evolving cracks. *Int J Numer Methods Eng* 61:2316–2343
- Ren H, Zhuang X, Cai Y, Rabczuk T (2016) Dual-horizon peridynamics. *Int J Numer Methods Eng* 108:1451–1476
- Rudnicki JW (1985) Effect of pore fluid diffusion on deformation and failure of rock. In: Bazant ZP (ed) *Mechanics of geomaterials*. Wiley, New York, pp 315–347
- Shi GH, Goodman RE (1985) 2 Dimensional discontinuous deformational analysis. *Int J Numer Anal Methods Geomech* 9:541–556
- Shimizu H, Murata S, Ishida T (2011) The distinct element analysis for hydraulic fracturing in hard rock considering fluid viscosity and particle size distribution. *Int J Rock Mech Min Sci* 48:712–727
- Shimizu H, Ito T, Tamagawa T, Tezuka K (2018) A study of the effect of brittleness on hydraulic fracture complexity using a flow-coupled discrete element method. *J Petrol Sci Eng* 160:372–383
- Terzaghi K (1951) *Theoretical soil mechanics*. Chapman and Hall, Limited, London
- Wang YT, Zhou XP, Kou MM (2018) Peridynamic investigation on thermal fracturing behavior of ceramic nuclear fuel pellets under power cycles. *Ceram Int* 44:11512–11542
- Weng L, Huang LQ, Taheri A, Li XB (2017) Rockburst characteristics and numerical simulation based on a strain energy density index: a case study of a roadway in Linglong gold mine, China. *Tunn Undergr Sp Technol* 69:223–232

- Wu Z, Wong LNY (2014) Extension of numerical manifold method for coupled fluid flow and fracturing problems. *Int J Numer Anal Methods Geomech* 38:1990–2008
- Wu Z, Fan L, Liu Q, Ma G (2017) Micro-mechanical modeling of the macro-mechanical response and fracture behavior of rock using the numerical manifold method. *Eng Geol* 225:49–60
- Wu Z, Xu X, Liu Q, Yang Y (2018) A zero-thickness cohesive element-based numerical manifold method for rock mechanical behavior with micro-Voronoi grains. *Eng Anal Bound Elem* 96:94–108
- Xia L, Yvonnet J, Ghabezloo S (2017) Phase field modeling of hydraulic fracturing with interfacial damage in highly heterogeneous fluid-saturated porous media. *Eng Fract Mech* 186:158–180
- Xie L, Min K-B, Shen B (2016) Simulation of hydraulic fracturing and its interactions with a pre-existing fracture using displacement discontinuity method. *J Nat Gas Sci Eng* 36:1284–1294
- Xing P, Yoshioka K, Adachi J, El-Fayoumi A, Damjanac B, Bungler AP (2018) Lattice simulation of laboratory hydraulic fracture containment in layered reservoirs. *Comput Geotech* 100:62–75
- Yan C, Jiao Y-Y (2018) A 2D fully coupled hydro-mechanical finite-discrete element model with real pore seepage for simulating the deformation and fracture of porous medium driven by fluid. *Comput Struct* 196:311–326
- Yan C, Zheng H, Sun G, Ge X (2015) Combined finite-discrete element method for simulation of hydraulic fracturing. *Rock Mech Rock Eng* 49:1389–1410
- Yang Y, Tang X, Zheng H, Liu Q, Liu Z (2018) Hydraulic fracturing modeling using the enriched numerical manifold method. *Appl Math Model* 53:462–486
- Zhang Y, Wong LNY (2018) A review of numerical techniques approaching microstructures of crystalline rocks. *Comput Geosci* 115:167–187
- Zhang HH, Li LX, An XM, Ma GW (2010) Numerical analysis of 2-D crack propagation problems using the numerical manifold method. *Eng Anal Bound Elem* 34:41–50
- Zhao GF, Zhao XB, Zhu JB (2014) Application of the numerical manifold method for stress wave propagation across rock masses. *Int J Numer Anal Methods Geomech* 38:92–110
- Zhao G, Kazerani T, Man K, Gao M, Zhao J (2015) Numerical study of the semi-circular bend dynamic fracture toughness test using discrete element models. *Sci China Technol Sci* 58:1587–1595
- Zheng H, Xu DD (2014) New strategies for some issues of numerical manifold method in simulation of crack propagation. *Int J Numer Methods Eng* 97:986–1010
- Zhou XP, Cheng H (2017) Multidimensional space method for geometrically nonlinear problems under total lagrangian formulation based on the extended finite-element method. *J Eng Mech* 143:04017036
- Zhou J, Zhang L, Pan Z, Han Z (2016) Numerical investigation of fluid-driven near-borehole fracture propagation in laminated reservoir rock using PFC 2D. *J Nat Gas Sci Eng* 36:719–733
- Zhou J, Zhang L, Pan Z, Han Z (2017) Numerical studies of interactions between hydraulic and natural fractures by smooth joint model. *J Nat Gas Sci Eng* 46:592–602
- Zhou XP, Wang YT, Shou YD, Kou MM (2018) A novel conjugated bond linear elastic model in bond-based peridynamics for fracture problems under dynamic loads. *Eng Fract Mech* 188:151–183
- Zhuang X, Augarde CE, Mathisen KM (2012) Fracture modeling using meshless methods and level sets in 3D: framework and modeling. *Int J Numer Methods Eng* 92:969–998

Publisher's Note Springer Nature remains neutral with regard to jurisdictional claims in published maps and institutional affiliations.